### **OPEN ACCESS**



# The 3D Kinematics of the Orion Nebula Cluster: NIRSPEC-AO Radial Velocities of the Core Population

Christopher A. Theissen <sup>1,4</sup>, Quinn M. Konopacky <sup>1</sup>, Jessica R. Lu<sup>2</sup>, Dongwon Kim<sup>2</sup>, Stella Y. Zhang <sup>1</sup>, Chih-Chun Hsu <sup>1</sup>, Laurie Chu <sup>3,5</sup>, and Lingfeng Wei <sup>1</sup>

<sup>1</sup> Center for Astrophysics and Space Sciences, University of California, San Diego, 9500 Gilman Drive, La Jolla, CA 92093, USA; ctheissen@ucsd.edu
<sup>2</sup> Department of Astronomy, University of California, Berkeley, Berkeley, CA 94720-3411, USA
<sup>3</sup> NASA Ames Research Center, Space Science and Astrobiology Division, Mail Stop 245-3, Moffett Field, CA 94035, USA
Received 2021 April 20; revised 2021 October 15; accepted 2021 October 19; published 2022 February 18

### **Abstract**

The kinematics and dynamics of stellar and substellar populations within young, still-forming clusters provide valuable information for constraining theories of formation mechanisms. Using Keck II NIRSPEC+AO data, we have measured radial velocities for 56 low-mass sources within 4' of the core of the Orion Nebula Cluster (ONC). We also remeasure radial velocities for 172 sources observed with SDSS/APOGEE. These data are combined with proper motions measured using HST ACS/WFPC2/WFC3IR and Keck II NIRC2, creating a sample of 135 sources with all three velocity components. The velocities measured are consistent with a normal distribution in all three components. We measure intrinsic velocity dispersions of  $(\sigma_{v_{\alpha}}, \sigma_{v_{\beta}}, \sigma_{v_{\gamma}}) = (1.64 \pm 0.12, 2.03 \pm 0.13, 2.56^{+0.16}_{-0.17})$  km s<sup>-1</sup>. Our computed intrinsic velocity dispersion profiles are consistent with the dynamical equilibrium models from Da Rio et al. (2014) in the tangential direction but not in the line-of-sight direction, possibly indicating that the core of the ONC is not yet virialized, and may require a nonspherical potential to explain the observed velocity dispersion profiles. We also observe a slight elongation along the north–south direction following the filament, which has been well studied in previous literature, and an elongation in the line-of-sight to tangential velocity direction. These 3D kinematics will help in the development of realistic models of the formation and early evolution of massive clusters.

*Unified Astronomy Thesaurus concepts:* Stellar kinematics (1608); Radial velocity (1332); Star formation (1569); Star forming regions (1565); Open star clusters (1160); Stellar associations (1582)

Supporting material: machine-readable tables

### 1. Introduction

The Orion Nebula Cluster (ONC) represents one of the best laboratories for studies of cluster formation and dynamics. Since the vast majority of stars are expected to form in clusters (Carpenter 2000; Lada & Lada 2003; Allen 2007), understanding cluster formation is of paramount importance to constraining star formation theory. The ONC is one of the closest ( $d \approx 390$  pc; Kounkel et al. 2017) examples of massive star formation, covering a large range of source masses (0.1–50  $M_{\odot}$ ; Hillenbrand 1997). There is also evidence to suggest that the cluster is not yet dynamically relaxed (Fűrész et al. 2008; Tobin et al. 2009), which is consistent with its youth ( $\sim$ 2.2 Myr; Reggiani et al. 2011).

Early studies of the kinematics of the ONC identified mass segregation, which is expected for young clusters (Hillenbrand 1997; Hillenbrand & Hartmann 1998). However, it remains an open question as to whether the observed mass segregation is primordial or dynamical. Given the estimated age of the ONC ( $\sim$ 2.2 Myr) and the cluster crossing time ( $\sim$ 2 Myr), it is thought that the mass segregation is primordial (Reggiani et al. 2011). However, these studies relied on a limited sample of 3D kinematic

Original content from this work may be used under the terms of the Creative Commons Attribution 4.0 licence. Any further distribution of this work must maintain attribution to the author(s) and the title of the work, journal citation and DOI.

information, largely resulting from the high level of extinction in the region (e.g., Johnson 1965; Walker 1983; Jones & Walker 1988; van Altena et al. 1988).

The largest-scale radial velocity (RV) studies of the ONC began with Fűrész et al. (2008) and Tobin et al. (2009), who observed 1215 and 1613 stars, respectively. These observations were taken using the Hectochelle multiobject echelle spectrograph (Szentgyorgyi et al. 1998) on the 6.5 m MMT telescope and the Magellan Inamori Kyocera Echelle (MIKE; Bernstein et al. 2003; Walker et al. 2007) on the Magellan Clay telescope. These fiberfed instruments obtain high-resolution ( $\lambda/\Delta\lambda\approx35,000$ ) optical (5150–5300 Å) spectra but are limited in their ability to observe stars in highly embedded regions and/or crowded fields (minimum separations of 30" for Hectochelle and 14" for MIKE). In particular, the core of the ONC—within 1' of the Trapezium—had poor coverage (five sources) due to the highly embedded and crowded nature of the core.

More recently, the Sloan Digital Sky Survey (SDSS; York et al. 2000), conducted an infrared (IR) survey of the ONC as part of SDSS-III (Eisenstein et al. 2011) using the Apache Point Observatory Galactic Evolution Experiment (APOGEE; Majewski et al. 2017) spectrograph (Da Rio et al. 2016, 2017). The APOGEE spectrograph (Wilson et al. 2010) on the Sloan 2.5 m telescope (Gunn et al. 1998) is a fiber-fed instrument that obtains H-band spectra (1.51–1.68  $\mu$ m) at a resolution of  $\lambda/\Delta\lambda\approx 22,500$ . This makes surveys using the APOGEE spectrograph less affected by extinction in embedded regions, but they are still limited in their ability to observe objects in crowded regions due to the 2'' diameter fibers. The most recent

<sup>&</sup>lt;sup>4</sup> NASA Sagan Fellow.

<sup>&</sup>lt;sup>5</sup> NASA Postdoctoral Program Fellow.

compilation of APOGEE measurements (APOGEE-II) was given in Kounkel et al. (2018, hereafter K18), which included measurements from the SDSS Data Release 12 (DR12; Alam et al. 2015) and Data Release 14 (DR14; Abolfathi et al. 2018). Authors of K18 presented high-precision ( $\sim$ 0.2 km s<sup>-1</sup>) RVs for 7774 sources in the ONC but only included 12 sources within 1' of the Trapezium.

Here we present a study of the 3D kinematics of the ONC sources within 4′ of the Trapezium. Our sample consists of 56 sources observed with NIRSPEC (McLean et al. 1998, 2000) on the Keck II 10 m telescope coupled with adaptive optics (AO) and a reanalysis of 172 sources observed with SDSS/APOGEE. This combined ONC sample represents the largest sample to date of RVs within the core of the ONC (≤1′; 41 sources). In Section 2, we discuss the literature data and new observations used in this study. Section 3 describes the methods used in reducing and forward-modeling the NIR-SPEC+AO (NIRSPAO) data. We discuss a reanalysis of the SDSS/APOGEE data using our forward-modeling pipeline in Section 4. A detailed study of the 3D kinematics of the ONC core is undertaken in Section 5. Lastly, a discussion of our results is given in Section 6.

### 2. Data

We obtained high-resolution near-IR (NIR) spectra of the sources closest to the core of the ONC—surrounding the Trapezium—using Keck/NIRSPAO between 2015 and 2020. Targets were initially chosen from a preliminary catalog of proper motions (PMs) computed using Keck Near Infrared Camera 2 (NIRC2; PI: K. Matthews) data. These sources were then cross-referenced with the Hillenbrand & Carpenter (2000) study of the low-mass members of the ONC. Figure 1 shows the targets of this study, as well as sources with RVs from the optical survey of (Tobin et al. 2009, hereafter T09) and the NIR survey using SDSS/APOGEE presented in K18. For the remainder of this study, we use the center-of-mass (CoM) coordinates determined by  $(\alpha_{\rm J2000}=05:35:16.26;$   $\delta_{\rm J2000}=-05:23:16.4;$  Da Rio et al. 2014) to represent the "center" of the ONC.

### 2.1. NIRSPAO Observations

All objects in our curated sample were observed using NIRSPEC on Keck II, in conjunction with the laser guide star (LGS) AO system (van Dam et al. 2006; Wizinowich et al. 2006). We used the instrument in its high spectral resolution AO mode with a slit width  $\times$  slit length of 0."041  $\times$  2."26. Observations were carried out in the *K* or *N*7 band to capitalize on the strong CO bands within that regime ( $\sim$ 2.3  $\mu$ m, orders 32 and 33). We additionally used a cross-disperser angle of 35°.65 and an echelle angle of 63°. The resolution in this setup is  $R \approx 25,000$ , as determined by the width of unresolved OH sky lines, and the wavelengths covered are approximately 2.044–2.075 (order 37), 2.100–2.133 (order 36), 2.160–2.193 (order 35), 2.224–2.256 (order 34), 2.291–2.325 (order 33), and 2.362-2.382 (order 32)  $\mu$ m, with some portions of the bands beyond the edges of the detector. For this work, all analysis was done using orders 32 and 33, the orders containing the CO bandheads in addition to numerous telluric features, and all NIRSPAO data presented come from these orders. We note that NIRSPEC underwent an upgrade during 2018, and our setup changed slightly postupgrade. The most significant

change is a larger wavelength coverage for each order due to a larger Hawaii 2RG detector (2048  $\times$  2048 postupgrade versus  $1024 \times 1024$  preupgrade; Martin et al. 2018) and a higher resolution ( $R \approx 35,000$ ; Hsu et al. 2021b).

Typical observations consisted of four spectra taken in an ABBA dither pattern along the length of the slit. In a few cases, more or less than four spectra were taken. Either before or after each target was observed, an A0V calibrator star at similar airmass was observed for a telluric reference. Table 1 gives the log of our spectroscopic observations, listing the targets observed, the date of observation, the number of spectra, and the integration time for each spectrum. Etalon lamp and flat-field frames were also taken each night for use in data reduction (Section 3).

### 3. NIRSPAO Reduction

Reduction of the NIRSPAO data was done using a modified version of the NIRSPEC Data Reduction Pipeline (NSDRP<sup>6,7</sup>). The NSDRP was specifically designed for point-source extraction and has been used extensively to obtain "quick looks" while observing at the Keck facility and for the Keck Observatory Archive (KOA; Berriman et al. 2005, 2010; Tran et al. 2012). Our updated version<sup>8</sup> includes the following modifications.

- 1. Use with the *K*-AO observing mode.
- 2. Spatial rectification using the object trace rather than the order edge traces.
- Spectral rectification and wavelength calibration using etalon lamps.
- 4. Cosmic-ray cleaning of flats.
- 5. Bad-pixel cleaning using methods ported from fix-pix\_rs.pro, which is a utility from REDSPEC (Kim et al. 2015; Prato et al. 2015).

In addition to the above modifications, we also removed fringes from the flat-field images prior to median-combining using the wavelet method of Rojo & Harrington (2006). This helps to mitigate beat patterns that can appear between fringing in the flats and science data.

Data for each night were reduced using standard procedures following the NSDRP documentation. We provide a summary of the steps involved in the reduction process here.

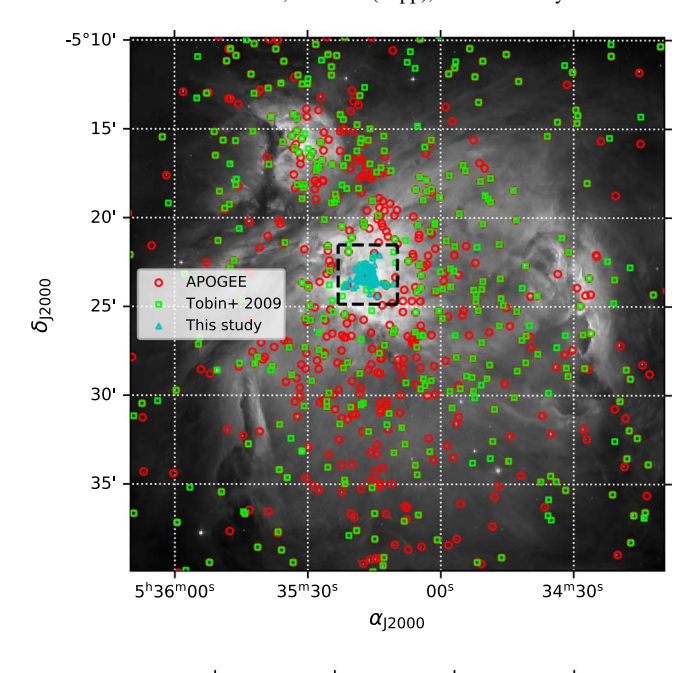
- 1. Flat frames are median-combined into a master flat frame.
- 2. The master flat is used to find order edges using predetermined dispersions based on the grating equation for NIPSPEC
- 3. Each frame (i.e., object, etalon/arc lamp) is cleaned for cosmic rays using Laplacian edge detection (van Dokkum 2001).
- Each frame is flat-normalized, and orders are extracted individually using the edge traces found from the master flat frame.
- Each order is cleaned for bad pixels using the fixpix routine.
- 6. Each order is spatially rectified using the object trace, determined by a Gaussian profile fit along each column.

https://www2.keck.hawaii.edu/koa/nsdrp/nsdrp.html

<sup>7</sup> https://github.com/Keck-DataReductionPipelines/NIRSPEC-Data-Reduction-Pipeline

<sup>8</sup> https://github.com/ctheissen/NIRSPEC-Data-Reduction-Pipeline

https://www2.keck.hawaii.edu/koa/nsdrp/nsdrp.html



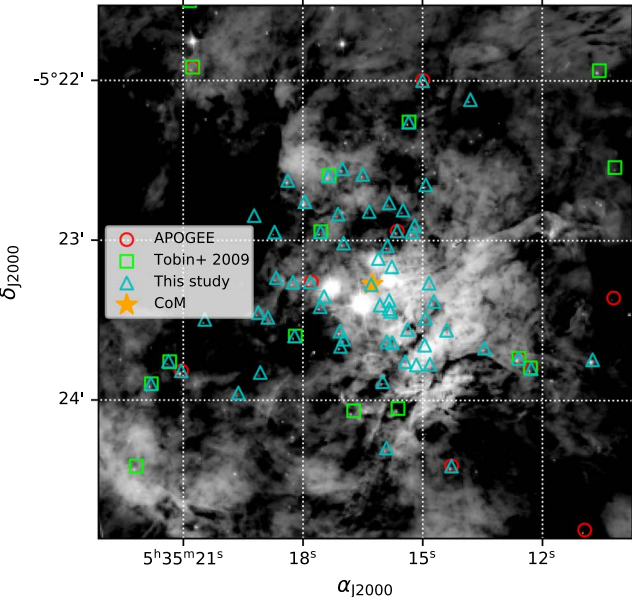


**Figure 1.** Top: HST ACS *R*-band image of the ONC (Robberto et al. 2013). Plotted are K18 APOGEE sources (red circles), T09 sources (green squares), and NIRSPAO sources from this study (cyan triangles). The black dashed box indicates the area shown in the bottom figure. Bottom: close-up image of the Trapezium. Sources are plotted with markers indicated in the legend. Our sources primarily represent the reddest sources closest to the Trapezium. The CoM coordinates from Da Rio et al. (2014) are indicated with the orange star.

- 7. Order edges are trimmed to remove bad pixels.
- 8. Each order is spectrally rectified using either the etalon or the arc lamp frame. The spectral trace is done by fitting Gaussians to the emission line traces and then finding the optimal spectral tilt (*y*-direction).
- 9. The object is extracted with box extraction, using optimal object and background regions found from Gaussian fits to the profile. The average sky (calculated using background regions adjacent to the 2D object spectrum) is subtracted from the object spectrum.
- Flux and noise are calculated using standard methods in the NSDRP.

Table 1
Log of NIRSPAO-LGS Observations

Target	Date of	A0V Star	Exposure Time	No. of	Filter
Name <sup>a</sup>	Obs. (UT)	Standard	$(s \times coadds)$	Frames	
HC 322	2015 Dec 23	HD 37887	$300 \times 1$	4	K
HC 296	2015 Dec 23	HD 37887	$1200 \times 1$	4	K
HC 259	2015 Dec 23	HD 37887	$90 \times 1$	4	K
HC 213	2015 Dec 23	HD 37887	$60 \times 1$	4	K
HC 306	2015 Dec 24	HD 37887	$180 \times 1$	4	K
HC 287	2015 Dec 24	HD 37887	$600 \times 1$	4	K
HC 291	2015 Dec 24	HD 37887	$600 \times 1$	4	K
HC 252	2015 Dec 24	HD 37887	$300 \times 1$	4	K
HC 250	2015 Dec 24	HD 37887	1200 × 1	4	K
HC 244	2015 Dec 24	HD 37887	$600 \times 1$	4	K
HC 244	2015 Dec 24 2015 Dec 24		$900 \times 1$	4	K
		HD 37887			
HC 248	2016 Dec 14	HD 37887	600 × 1	4	K
HC 223	2016 Dec 14	HD 37887	$300 \times 1$	4	K
HC 219	2016 Dec 14	HD 37887	$600 \times 1$	4	K
HC 324	2016 Dec 14	HD 37887	$1200 \times 1$	3	K
HC 295	2018 Feb 11	HD 37887	$450 \times 1$	5	K
HC 313	2018 Feb 11	HD 37887	$180 \times 1$	4	K
HC 332	2018 Feb 11	HD 37887	$300 \times 1$	4	K
HC 331	2018 Feb 11	HD 37887	$450 \times 1$	4	K
HC 337	2018 Feb 11	HD 37887	$60 \times 1$	4	K
HC 375	2018 Feb 11	HD 37887	$180 \times 1$	4	K
HC 338	2018 Feb 11	HD 37887	120 × 1	4	K
HC 425	2018 Feb 12	HD 37887	$60 \times 1$	4	K
HC 713	2018 Feb 12	HD 37887	$90 \times 1$	4	K
HC 408	2018 Feb 12	HD 37887	$450 \times 1$	4	K
HC 410	2018 Feb 12	HD 37887	600 × 1	4	K
HC 436	2018 Feb 12	HD 37887	90 × 1	4	K
HC 442	2018 Feb 13	HD 37887	$450 \times 1$	4	K
HC 344	2018 Feb 13	HD 37887	$60 \times 1$	4	K
HC 522	2019 Jan 12	HD 37887	$450 \times 1$	4	K
HC 145	2019 Jan 12	HD 37887	$600 \times 1$	4	K
HC 202	2019 Jan 12	HD 37887	$120 \times 1$	4	K
HC 188	2019 Jan 12	HD 37887	$600 \times 1$	4	K
HC 302	2019 Jan 13	HD 37887	$450 \times 1$	4	<i>N</i> 7
HC 275	2019 Jan 13	HD 37887	$450 \times 1$	2	<i>N</i> 7
HC 245	2019 Jan 13	HD 37887	$180 \times 1$	4	<i>N</i> 7
HC 258	2019 Jan 13	HD 37887	$180 \times 1$	4	<i>N</i> 7
HC 344	2019 Jan 13	HD 37887	$120 \times 1$	4	<i>N</i> 7
HC 370	2019 Jan 16	HD 37887	180 × 1	4	N7
HC 389	2019 Jan 16	HD 37887	120 × 1	4	N7
HC 386	2019 Jan 16	HD 37887	$120 \times 1$	4	N7
	2019 Jan 16	HD 37887		4	
HC 398			120 × 1		N7
HC 413	2019 Jan 16	HD 37887	180 × 1	4	N7
HC 253	2019 Jan 16	HD 37887	120 × 1	4	N7
HC 288	2019 Jan 17	HD 37887	450 × 1	4	N7
HC 420	2019 Jan 17	HD 37887	$450 \times 1$	4	<i>N</i> 7
HC 412	2019 Jan 17	HD 37887	$450 \times 1$	4	<i>N</i> 7
HC 288	2019 Jan 17	HD 37887	$450 \times 1$	4	<i>N</i> 7
HC 282	2019 Jan 17	HD 37887	$450 \times 1$	3	<i>N</i> 7
HC 277	2019 Jan 17	HD 37887	$180 \times 1$	4	<i>N</i> 7
HC 217	2020 Jan 18	HD 37887	$120 \times 1$	4	<i>N</i> 7
HC 229	2020 Jan 18	HD 37887	$450 \times 1$	4	<i>N</i> 7
HC 229	2020 Jan 18	HD 37887	$450 \times 1$	4	<i>N</i> 7
HC 228	2020 Jan 19	HD 37887	$120 \times 1$	4	N7
HC 224	2020 Jan 19	HD 37887	90 × 1	4	N7
HC 135	2020 Jan 19	HD 37887	$180 \times 1$	4	N7
HC 440	2020 Jan 20	HD 37887	$120 \times 1$	4	N7
HC 450	2020 Jan 20	HD 37887	$300 \times 1$	4	N7
HC 277	2020 Jan 20	HD 37887	$300 \times 1$	4	N7
HC 204	2020 Jan 20	HD 37887	$300 \times 1$	4	N7
HC 229	2020 Jan 20	HD 37887	$450 \times 1$	4	<i>N</i> 7
HC 214	2020 Jan 20	HD 37887	$450 \times 1$	4	<i>N</i> 7
HC 215	2020 Jan 21	HD 37887	$300 \times 1$	4	<i>N</i> 7

Table 1 (Continued)

Target Name <sup>a</sup>	Date of Obs. (UT)	A0V Star Standard	Exposure Time $(s \times coadds)$	No. of Frames	Filter
HC 240	2020 Jan 21	HD 37887	300 × 1	4	N7
HC 546	2020 Jan 21	HD 37887	$300 \times 1$	4	<i>N</i> 7
HC 504	2020 Jan 21	HD 37887	$120 \times 1$	4	<i>N</i> 7
HC 703	2020 Jan 21	HD 37887	$300 \times 1$	4	<i>N</i> 7
HC 431	2020 Jan 21	HD 37887	$120 \times 1$	3	<i>N</i> 7
HC 229	2020 Jan 21	HD 37887	$450 \times 1$	2	<i>N</i> 7

### Note.

 The wavelength solution is calibrated for each order using a synthesized etalon or sky spectrum and fitting to lines found in each order.

Initial wavelength solutions were obtained by mapping pixels to the etalon lamp wavelengths; however, etalon lamps only provide uniform spacing in the frequency domain, with the initial absolute or starting position unknown. For example, it is unknown whether the first etalon fringe starts at 20000 Å or 20010 Å, but the spacing of  $c\lambda^{-1}$  is absolute. Therefore, the wavelength solution is recalibrated using telluric features within each frame, which are anchored to an absolute rest frame, as part of our forward-modeling framework (Section 3.1).

### 3.1. Forward-modeling NIRSPEC Data

Our data were forward-modeled using the Spectral Modeling Analysis and RV Tool (SMART;<sup>10</sup> Hsu et al. 2021a). Details for the fitting routine using SMART are given in Hsu et al. (2021b). Here we briefly outline our methods.

Reduced NIRSPAO data were modeled using an iterative approach. The first step was obtaining an absolute wavelength solution to orders 32 and 33. For our initial wavelength solution, we use the global wavelength solution provided by the NSDRP, which is a quadratic polynomial<sup>11</sup> of the form

$$\lambda(p, M) = r_0 + r_1 p + r_2 p^2 + \frac{r_3}{M} + \frac{r_4 p}{M} + \frac{r_5 p^2}{M}, \quad (1)$$

where  $\lambda(p, M)$  is the wavelength falling on column pixel p of order M and coefficients  $r_n$ . This initial wavelength solution is obtained from fitting to the etalon lamps, which provides uniform offsets in frequency space. However, as mentioned previously, the absolute wavelength solution, or starting position, is unknown for the etalon spectrum.

To obtain a more precise wavelength calibration, we performed a cross-correlation between our telluric spectrum from the A-star calibrator to the high-resolution telluric spectrum from Moehler et al. (2014). First, we modeled and removed the continuum of our A-star calibrator using a quadratic polynomial, essentially leaving just the flat imprinted telluric absorption spectrum. Then, we scaled the flux of the high-resolution telluric model to the A-star flux. Next, the telluric spectrum from the A0V star was cross-correlated with the telluric model using a window of

100 pixels and a step size of 20 pixels, calculating the best-fit cross-correlation shift for each window along the entire spectrum. Then, a fourth-order polynomial—i.e.,  $\lambda(p) = a_i + b_i p + c_i p^2 +$  $d_i p^3 + e_i p^4$ , where i is the iteration number—was fit to the best wavelength shifts for all windows used in that iteration. The initial wavelength solution was given using the second-order polynomial provided by the NSDRP, with the additional coefficients set to zero (i.e.,  $d_0$ ,  $e_0$ ). The best-fit coefficients for each pass (e.g.,  $\delta_{a_0}$ ) were added to the previous solution, e.g.,  $a_1 = a_0 + \delta_{a_1}$ ,  $b_1 = b_0 + \delta_{b_1}$ . This loop was repeated until the wavelength solution converged to the smallest residuals between the telluric spectrum and telluric model. One thing to note is that different iterations used a different pixel window and step size, as finer granularity is required as the wavelength solution gets closer to the optimal fit. For instance, the second pass used a step size of 10 pixels and a window size of 150 pixels.

The aforementioned fitting procedure was done for each frame independently, resulting in an absolute wavelength solution for each frame. We cross-correlated a single A-star frame to A-star calibration data taken over 14 nights (both A and B nods) and found an rms between frames of 0.004 Å (0.058 km s<sup>-1</sup>). Although this systematic uncertainty is typically much smaller than our measurement uncertainty, we add this systematic in quadrature with our measurement uncertainties per frame.

Next, we modeled the spectrum using a forward-modeling approach based on the method provided by Blake et al. (2010) and also Butler et al. (1996), Blake et al. (2007, 2008, 2010), and Burgasser et al. (2016), utilizing a Markov Chain Monte Carlo (MCMC) method built on *emcee* (Foreman-Mackey et al. 2013) to sample the parameter space.

The flux from the source can be modeled using the following equation:

$$F_{M}[p] = C[p(\lambda)] \times \left[ \left( M \left[ p^{*} \left( \lambda \left[ 1 + \frac{V_{r}}{c} \right] \right), T_{\text{eff}}, \log g, [M/H] \right] \right) \right]$$

$$*\kappa_R(v \sin i) + C_{\text{veil}}) \times T[p^*(\lambda), \text{AM, PWV}]$$

$$*\kappa_G(\Delta \nu_{\text{inst}}) + C_{\text{flux}},$$
(2)

where an asterisk indicates convolution,  $C[p(\lambda)]$  is a quadratic polynomial that is used for continuum correction (meant to correct and scale for variations induced by the instrumental profile on the observed and absolute flux of the model), and M is the photospheric model of the source. We fixed  $\log g = 4$ , as this is approximately the expected gravity for low-mass stars at the age of the ONC that are still contracting onto the main sequence and consistent with other studies (e.g., Kounkel et al. 2018). Additionally, we show later that RV variations with  $\log g$  tend to be small. We also fixed [M/H] = 0 based on the average metallicity of the ONC (e.g., D'Orazi et al. 2009). Here  $\kappa_R(v \sin i)$  is the rotational broadening kernel (using the methods of Gray 1992 and a limb-darkening coefficient of 0.6);  $V_r$  and c are the heliocentric RV and speed of light, respectively; T is the telluric spectrum from Moehler et al. (2014); and AM and PWV are the airmass and precipitable water vapor of the telluric spectrum, respectively. Veiling is parameterized by  $C_{\text{veil}}$ , which is an additive graybody flux to the stellar model flux (continuum),  $r_{\lambda} = F_{\lambda,\text{cont}}/F_{\lambda,*}$  (or

<sup>&</sup>lt;sup>a</sup> Identifier from Hillenbrand & Carpenter (2000).

<sup>10</sup> https://github.com/chihchunhsu/smart

<sup>11</sup> https://www2.keck.hawaii.edu/koa/nsdrp/documents/NSDRP\_Software\_Design.pdf

Table 2
Forward-modeled Parameter Ranges

Description	Symbol	Bounds
Stellar effective temp.	$T_{ m eff}$	(2300, 7000) K
Rotational velocity	v sin i	$(1, 100) \text{ km s}^{-1}$
RV	$V_r$	$(-100, 100) \text{ km s}^{-1}$
Airmass	AM	(1, 3)
Precip. water vapor	PWV	(0.5, 30) mm
LSF	$\Delta  u_{ m inst}$	$(1, 100) \text{ km s}^{-1}$
Flux offset param.	$C_{ m flux}$	$(10^{-15}, 10^{15})$ counts s <sup>-1</sup>
Noise factor	$C_{ m noise}$	(1, 50)
Wave. offset param.	$C_{\lambda}$	(-10, 10)  Å

 $C_{\text{veil}}/F_{\lambda,*}$ ), to represent potential veiling along the line of sight, which will weaken the depths of the photospheric absorption lines (e.g., Muzerolle et al. 2003a, 2003b; Fischer et al. 2011). Extinction effects, which reduce the intensity of the emission lines, are multiplicative in nature and therefore get folded into the fit for  $C[p(\lambda)]$ . We note that due to the small range of wavelengths used, effects due to extinction should be minimal and would mostly impact stellar parameters, rather than RVs.

Here  $p^* = p(\lambda) + C_{\lambda}$ , where  $p(\lambda)$  is a fourth-order polynomial mapping of pixel to wavelength based on the telluric spectrum from the absolute wavelength calibration to the A star, and  $C_{\lambda}$  is a small constant offset/correction to the zerothorder term. We keep constant all coefficients in the fourth-order polynomial that were derived from the A-star calibrator, save for the zeroth-order term, which we fit for a small constant offset (nuisance parameter) to account for small differences in the absolute wavelength calibration versus the observed data. This is necessary, as observations not taken along the exact same pixels will shift by a small amount due to the spatial curvature of the flux along the detector. Here  $\kappa_G(\Delta\nu_{\rm inst})$  is the spectrograph line-spread function (LSF), modeled as a normalized Gaussian. We include an additive flux offset,  $C_{\text{flux}}$ , as an additional nuisance parameter to account for small differences in the absolute flux calibration. We fit for separate  $C_{\lambda}$  and  $C_{\text{flux}}$ parameters for each order. For stellar models, we chose the PHOENIX-ACES-AGSS-COND-2011 stellar models (Husser et al. 2013), which have been used previously for modeling ONC young stellar objects (YSOs) observed in the NIR with SDSS/APOGEE (Kounkel et al. 2018)

The log-likelihood function, assuming normally distributed parameters and noise, is

$$\ln \mathcal{L} = -\frac{1}{2} \sum_{p} \left[ \left( \frac{D[p] - F_M[p]}{\sigma[p] \times C_{\text{noise}}} \right)^2 + \ln[2\pi(\sigma[p] \times C_{\text{noise}})^2] \right], \tag{3}$$

where D[p] is the data,  $\sigma[p]$  is the noise or flux uncertainty, and  $C_{\text{noise}}$  is a scaling parameter for the noise to account for systematic errors between the observations and the models.

We simultaneously fit for all of the above parameters, using the affine-invariant ensemble sampler *emcee*, with the kerneldensity estimator described in Farr et al. (2014). Uniform priors were used across the parameter ranges shown in Table 2. We did an initial fit using 100 walkers and 400 steps, discarding the first 300 steps. Typical convergence occurred after the initial 200 steps. These fits were then masked for bad pixels outside of

three standard deviations of the median difference between the model and the data, effectively removing bad pixels and cosmic rays that were not removed by the fixpix utility. Next, another fit was performed on the masked data with 100 walkers, 300 steps, and a burn-in of 200 steps. Walkers were initialized within 10% of the best-fit parameters from the initial fit. Convergence typically occurred within 100 steps. Heliocentric RVs were corrected for barycentric motion using the *astropy* function radial\_velocity\_correction.

An example fit is shown in Figure 2, with the observed telluric-corrected-spectrum shown with the gray line, the best-fit stellar model shown with the red line (model parameters indicated in red text), and the best-fit stellar model convolved with the best-fit telluric model shown with the purple line. The gray spectrum and purple model are compared in our MCMC routine. The bottom plots show the residuals between the observed spectrum and best-fit model (black line) and the total uncertainty (noise computed from the NSDRP with the scaling factor in Equation (3)). The largest contributor to the residuals is fringing, which is an ongoing project to model and will be addressed in a future study. However, previous studies of modeling NIRSPEC fringing have shown that it does not significantly effect RV determinations (Blake et al. 2010). Figure 3 shows the corner plot for the MCMC run for Figure 2 (last  $100 \text{ steps} \times 100 \text{ walkers}$ , 10,000 data points). The parameters listed on the x- and y-axes are the same as those from Equations (2) and (3). This plot indicates that there is little to no correlation between the majority of parameters, with the exception of  $v \sin i$  and veiling, which show a slight correlation. As can be seen, some of these distributions are non-Gaussian, which is why we report median values with 16th and 84th percentiles as uncertainties. The results of our fits are listed in

Many of our sources converged to relatively high veiling parameters (i.e.,  $r_{\lambda} > 0.2$ ), and we note that temperature should be highly degenerate with veiling ratio due to the strong dependence of the fits on the CO bands, which could be weakened either by higher effective temperatures or higher veiling ratios. However, we do not have sufficient data to put constraints on the veiling parameter for each source, as that would required a 3D extinction map of the ONC (e.g., Schlafly et al. 2015) and precise distances to individual sources. However, even with the Gaia satellite (Gaia Collaboration et al. 2016), the embedded nature of the ONC makes parallax measurements extremely difficult (Kim et al. 2019). Therefore, this study is focused on the kinematics of the ONC; however, a future study will investigate the  $T_{\rm eff}$  (and mass) dependence of kinematics in the ONC core.

Our RV measurements are relatively robust to changes in stellar parameters, since they are strongly anchored to the CO bandheads and the absolute calibration of the telluric spectrum. To illustrate this, we fit [HC 2000] 244 (the same source shown in Figure 2) using the same procedure outlined above and holding the  $\log g$  constant from zero to 6 in steps of 0.5 (the resolution of the model grid). Figure 4 (top) shows the RV variation due to different  $\log g$  values. For  $\log g$  values that differ by more than  $\pm 1$  dex from the nominal value, RV variations are more than 1%; however, those are extremely large variations in  $\log g$  that are inconsistent with the youth of these targets. For RV values within  $\pm 0.5$  dex, the variation is less than 0.5%. To be conservative, we chose to add this

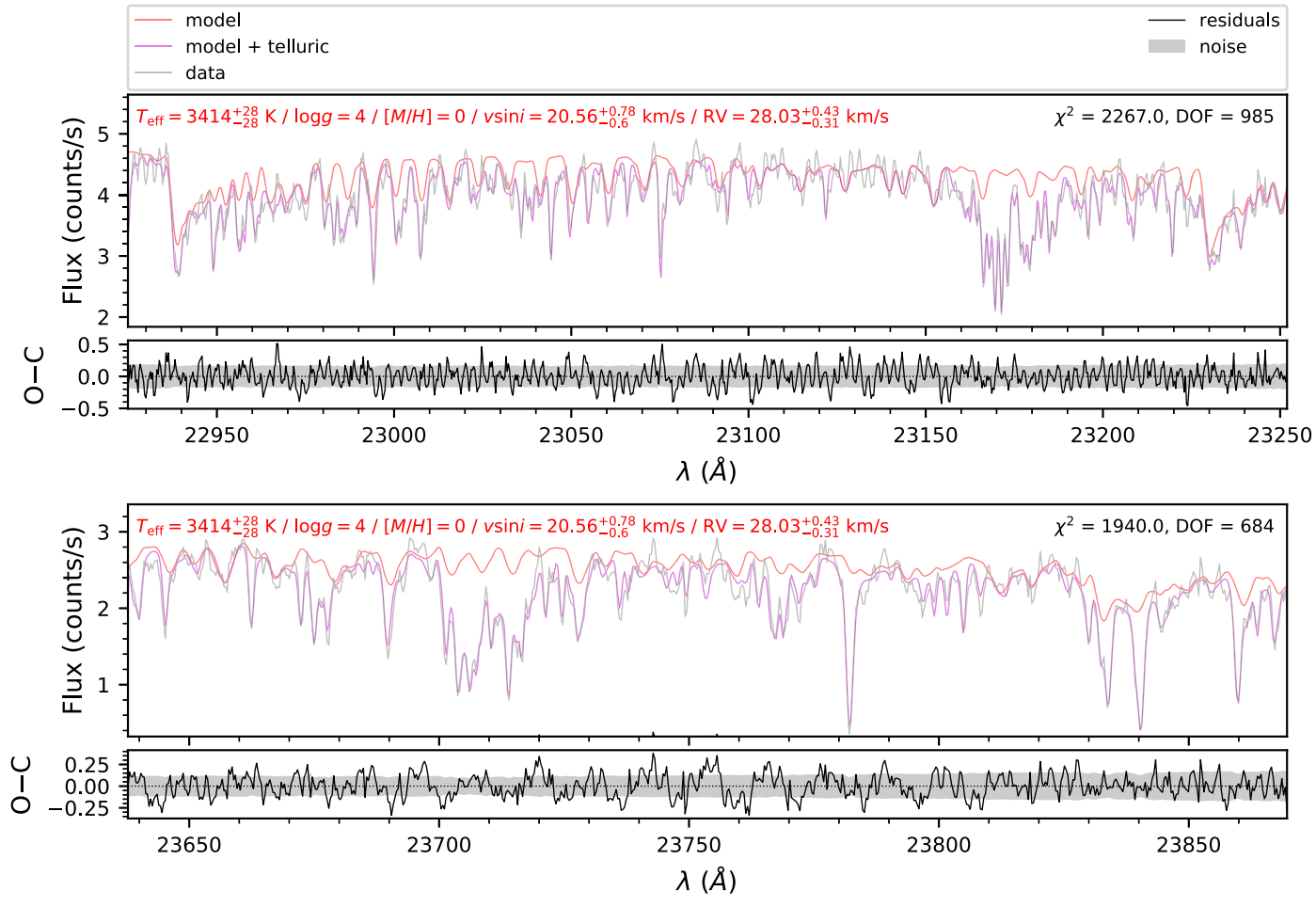


Figure 2. Best-fit forward model of a single frame for [HC 2000] 244, orders 33 (top) and 32 (bottom). Plotted are the data (light gray lines), stellar model (red lines), and stellar model multiplied by the telluric spectrum (purple lines). The bottom plot under each order shows the residuals (black lines) and the uncertainty in the flux (gray shaded regions). The best-fit parameters are listed in the top right corners, with  $\log g$  and metallicity ([M/H]) fixed at 4 and zero, respectively. The residuals are dominated by fringing.

systematic uncertainty to our combined measurement uncertainty across all frames for each single object.

We performed a similar test to the one above, this time holding temperature constant. Figure 4 (bottom) shows the RV variation due to different temperatures. Within a few hundred kelvins, the RV variation is less than 3%. However, within  $\pm 100$  K, this value is less than 0.5%, which is within the systematic uncertainty found in the  $\log g$  variation. Therefore, no additional systematic is required, since the  $\pm 0.5\%$  systematic accounts for both the  $\log g$  and  $T_{\rm eff}$  variations. In summary, our reported uncertainties are the summed quadrature of our measurement uncertainty from the MCMC fits, the 0.058 km s $^{-1}$  systematic uncertainty between calibration frames, and the 0.5% variation found from differing  $\log g$  and  $T_{\rm eff}$ .

Lastly, we compare our derived RVs to those from APOGEE (using the results of K18) and Tobin et al. (2009), using the reanalyzed RVs from Kounkel et al. (2016, hereafter K16). Figure 5 shows the results of our RV comparison. In total, there were 11 matches between our NIRSPEC targets and the T09/K16 sample and seven matches to APOGEE (using a 0."5 crossmatch radius). Our results are consistent with the K18 APOGEE results, with only two exceptions differentiating by more than  $1\sigma$  of their combined uncertainty, possibly the result of spectroscopic

binaries: 2MASS J05352104–0523490 and 2MASS J05351498 –0521598. In comparison to optical RVs from T09/K16, our measured RVs are generally smaller than those measured from optical data, by  $\sim\!1.8$  km s $^{-1}$ , on average. We also compared K16 to K18 RVs, again using a 0."5 crossmatch radius, finding 586 sources in common (Figure 5, green symbols). The distribution of the uncertainty-weighted difference between these two measurements,  $(RV_{K18}-RV_{K16})/\sqrt{\sigma_{RV_{K18}}^2+\sigma_{RV_{K16}}^2}$ , has a mean value of  $\mu=0.58$  km s $^1$  and a standard deviation of  $\sigma=1.83$  km s $^1$ . This is consistent with the K16 values being, on average, smaller than the K18 APOGEE RVs. The width of the distribution also indicates that one or both of the uncertainties are underestimated. In general, RVs derived from NIR data versus optical are likely to suffer from fewer systematics in this highly embedded region.

### 4. APOGEE Reanalysis

It is useful to assess the fidelity of the parameters derived in our pipeline by applying it to an independent data set. We chose to apply our pipeline to the APOGEE H-band data. These data have independent measurements of  $T_{\rm eff}$ , log g, and RVs of ONC sources from K18. We chose to do a subset of the entire K18 catalog, selecting objects within 4' of the ONC CoM

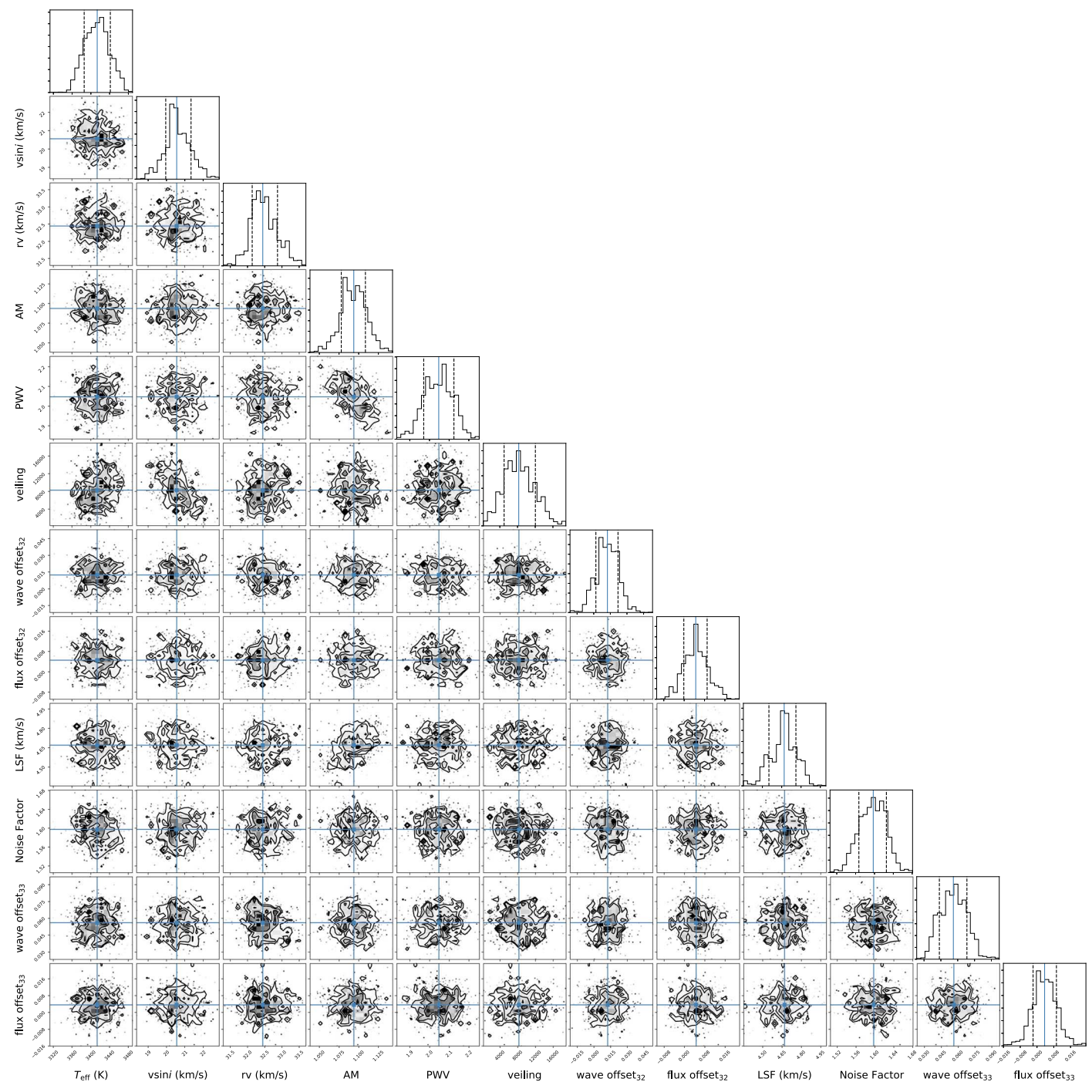


**Figure 3.** Corner plot of a single frame for [HC 2000] 244. This corner plot corresponds to the fit in Figure 2. The subscripts in the parameter labels refer to the orders. The solid line shows the median of each distribution, and the dotted lines show the 16th and 84th percentiles.

(172 sources). We used a similar version of our aforementioned pipeline (see Section 3.1), with the flux for each chip modeled using Equation (2). The LSF was modeled as a sum of Gauss–Hermite functions (Nidever et al. 2015) obtained using the *apogee*<sup>12</sup> code (Bovy 2016). It should be noted that our model choice of PHOENIX-ACES-AGSS-COND-2011 (Husser et al. 2013) is the same as that used in K18.

We fit all three chips simultaneously (A: 1.647– $1.696~\mu m$ ; B: 1.585– $1.644~\mu m$ ; and C: 1.514– $1.581~\mu m$ ), allowing each chip to

have separate nuisance parameters (e.g.,  $C0_{\rm flux,A}$  and  $C1_{\rm flux,A}$  for chip A,  $C0_{\rm flux,B}$  and  $C1_{\rm flux,B}$  for chip B), similar to our simultaneous modeling of separate NIRSPEC orders. An example fit is shown in Figure 6. In general, the APOGEE sources tend to be much brighter than our NIRSPEC sources; however, the median H-band veiling ratio for APOGEE sources is 0.58, and these sources are more susceptible to confusion due to the size of the fiber (2" diameter; Majewski et al. 2017). The results of our fits are listed in Table 5, including measured veiling ratios and noting sources where a nearby companion could confuse the results. We show comparisons of our derived  $T_{\rm eff}$  and RVs to

<sup>12</sup> https://github.com/jobovy/apogee

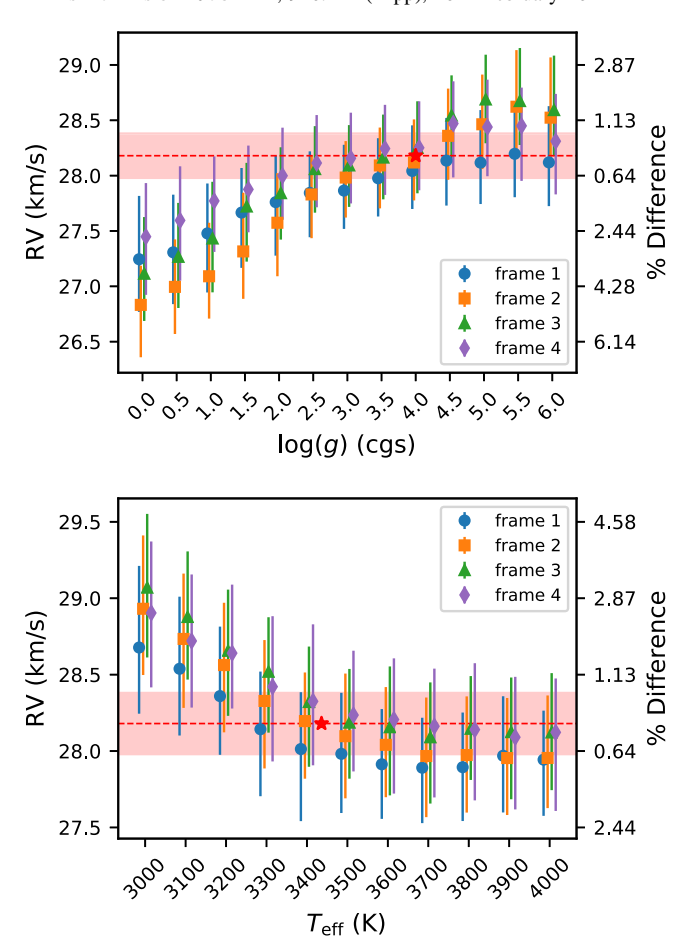


**Figure 4.** Best-fit RVs for [HC 2000] 244 while keeping  $\log g$  (top) and temperature (bottom) constant. Each marker shows one of the four frames. In the top panel, the RV variation within  $\log g \pm 0.5$  dex of our adopted values (28.18 km s<sup>-1</sup> and  $\log g = 4$ ; red star and dashed line, with uncertainties shown by the shaded area) is less than 1%. Even at much lower/higher gravities, the RV variation is not more than a few percent. At the age of the ONC, the expected surface gravity values are  $\log g \sim 3$ –4. In the bottom panel, the RV variation within a few hundred kelvins of our adopted values (28.18 km s<sup>-1</sup> and 3436 K; red star and dashed line, with uncertainties shown by the shaded area) is less than a few percent.

those from K18 in Figure 7. Our derived temperatures are overall consistent with K18, although there is a small systematic shift from low to high temperatures. Our RVs are consistent with those from K18 ( $\overline{\Delta}$ RV = 0.23 ± 0.43 km s<sup>-1</sup>), with a number of sources having measured RVs where K18 only provided upper limits. In total, we provide RV measurements for 87 sources that previously had no measurement in K18. We note that although these sources have no definitive measurement in K18, many of them have RV measurements from the SDSS/APOGEE processing pipeline (Nidever et al. 2015). However, K18 mentioned that these estimates tend to be unreliable for sources with  $T_{\rm eff}$  < 3000 K, and potentially also for YSOs, where veiling must be accounted for.

### 5. The Kinematic Structure of the ONC Core

The 3D kinematic studies of the ONC core have been primarily focused on the Trapezium stars, as they are the brightest objects in the highly embedded region (e.g., Olivares et al. 2013). From Figure 1, it can be seen that very few previous studies have obtained RVs for sources within the

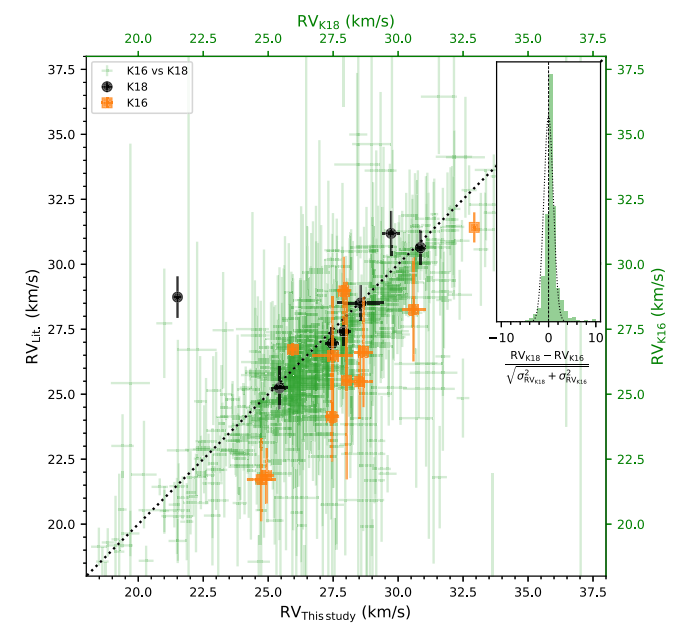


**Figure 5.** Comparison between NIRSPEC RVs from this study and APOGEE RVs from K18 (black circles) and optical RVs from K16 (orange squares). We show K16 vs. K18 with translucent green symbols (662 sources). The black dotted line indicates where RV measurements are equal. The large outlier, [HC 2000] 546, is a potential RV variable binary. The inset plot shows the distribution of  $(RV_{K18} - RV_{K16}) / \sqrt{\sigma_{RV_{K18}}^2 + \sigma_{RV_{K16}}^2}$ , which has  $\mu = 0.58$  and  $\sigma = 1.83$  km s<sup>-1</sup>. This indicates that the K16 RVs are, on average, smaller than the K18 APOGEE RVs, and that the uncertainties in at least one of the surveys are underestimated. The inset plot shows a normal distribution with  $\mu = 0$  and  $\sigma = 1$  for comparison (dotted line).

direct vicinity of the Trapezium stars. Here we analyze the 3D kinematics of sources that make up the "core" of the ONC.

### 5.1. Tangential Velocities

Our measurements provide velocities along the line of sight; however, to measure 3D velocities, we require tangential motions. A number of studies have measured the PMs of sources within the ONC (e.g., Parenago 1954; Jones & Walker 1988; van Altena et al. 1988; Gómez et al. 2005; Dzib et al. 2017; Kim et al. 2019; Kuhn et al. 2019; Platais et al. 2020). The two most recent catalogs produced by Kim et al. (2019) and Platais et al. (2020) both use imaging data from the Hubble Space Telescope (HST). We chose to adopt the values from Kim et al. (2019), as their combination of HST imaging with data from the Keck Near Infrared Camera 2 (NIRC2; PI: K. Matthews) provides a baseline of  $\sim$ 20 yr. Additionally, the uncertainties published by Platais et al. (2020) tend to be very small and are possibly underestimated due to the fact that they were unable to determine systematic uncertainties. This likely explains their much smaller errors versus Kim et al. (2019), even though a shorter time baseline of  $\sim$ 11 yr was used.

The Kim et al. (2019) catalog includes PM measurements for 701 sources with typical uncertainties ≤1 mas yr<sup>-1</sup>. However, to convert PMs into tangential velocities, we require a distance, or distance distribution, to the ONC. A number of studies have investigated the distance to the ONC using very long baseline interferometry (VLBI; Menten et al. 2007; Sandstrom et al. 2007; Kounkel et al. 2017) and, more recently, the Gaia Data Release 2 (DR2; Gaia Collaboration et al. 2018; Großschedl et al. 2018; Kounkel et al. 2018; Kuhn et al. 2019). The majority of these measurements are consistent with an average distance to the ONC

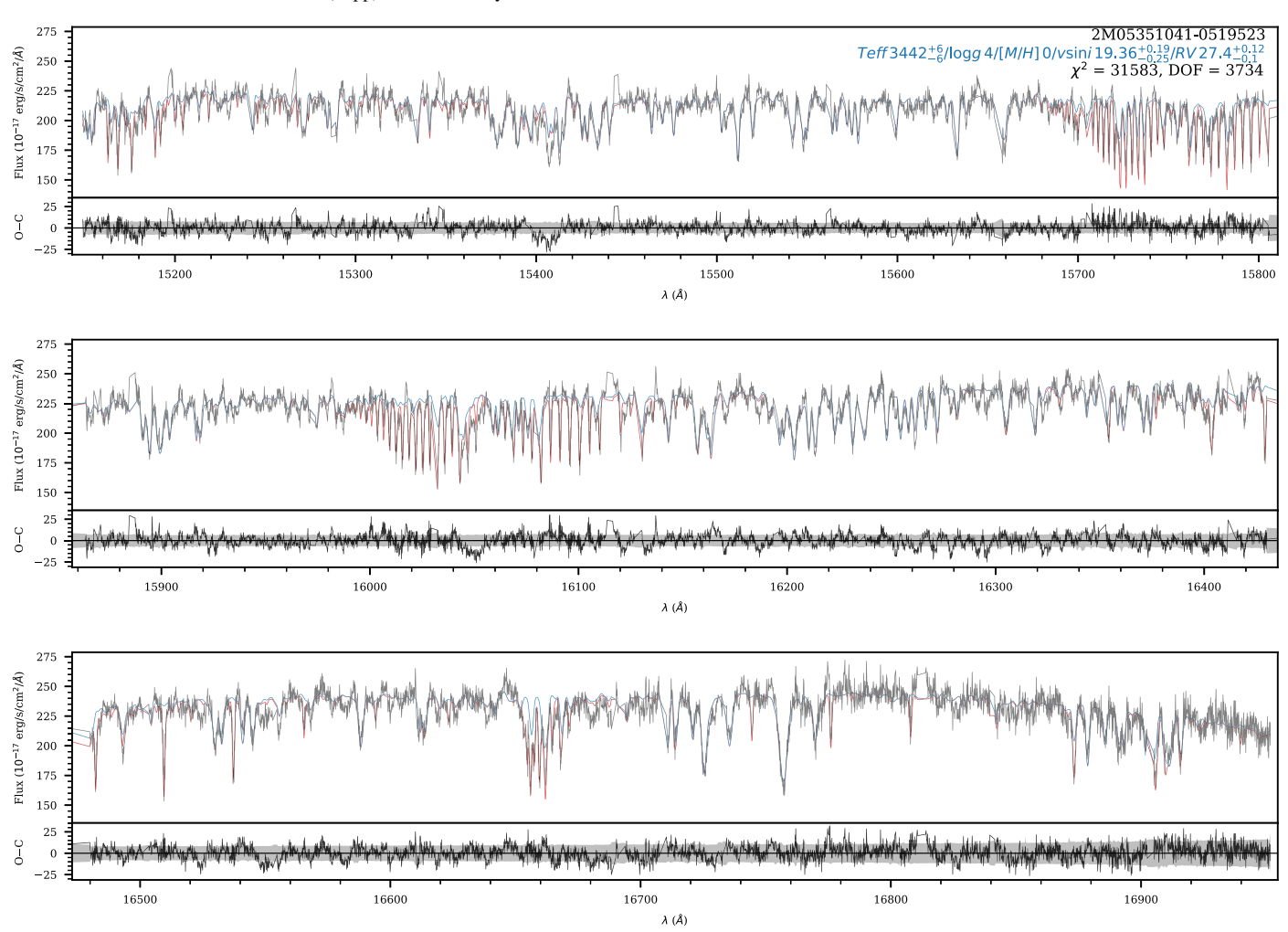


Figure 6. Example fit to APOGEE data for all three chips. Raw APOGEE data are shown in gray, the best-fit stellar model is shown in blue (parameters given in the upper right corner), and the best-fit stellar model convolved with the best-fit telluric model is shown in red. Residuals are shown in the lower plot (black line), along with the flux uncertainty (gray shaded region).

of  $\sim$ 390 pc. For our study, we adopted the VLBI trigonometric distance of  $388 \pm 5$  pc from Kounkel et al. (2017), which is consistent with Kounkel et al. (2018;  $389 \pm 3$  pc, Gaia DR2), Kuhn et al. (2019;  $403^{+7}_{-6}$  pc, Gaia DR2), Großschedl et al. (2018;  $397 \pm 16$  pc, Gaia DR2), and Sandstrom et al. (2007;  $389^{+24}_{-21}$  pc, VLBI).

Using the above distance estimate, we converted PMs to tangential velocities, combining errors in PMs and the distance to the ONC using standard error propagation. The combined sample with all three components of motion totaled 135 sources. Figure 8 shows a map of the ONC with vectors displaying the PM of sources in our sample and colors representing the measured RVs. All three components of motion for our subsample are shown in Figure 9. These velocities were used to investigate the 3D kinematics of the ONC core region. There are a number of kinematic outliers, both in tangential velocity space (as discussed in Kim et al. 2019) and in RV space, that will be discussed in Section 5.3.

### 5.2. Intrinsic Velocity Dispersion Calculation

To determine velocity dispersion, we utilized a similar Bayesian framework to Kim et al. (2019), where each *i*th kinematic measurement is parameterized as  $v_{(\alpha,\delta,r)_i} \pm \epsilon_{(\alpha,\delta,r)_i}$ . We

assume each kinematic measurement is drawn from a multivariate Gaussian distribution with mean values of  $\bar{\nu}_{\alpha}$ ,  $\bar{\nu}_{\delta}$ , and  $\bar{\nu}_{r}$  and standard deviations of  $\sqrt{\sigma_{\nu_{(\alpha,\delta,r)}}^2 + \epsilon_{(\alpha,\delta,r)_i}^2}$ , where  $\sigma_{\nu_{\alpha}}$ ,  $\sigma_{\nu_{\delta}}$ , and  $\sigma_{\nu_{r}}$  are the intrinsic velocity dispersions (IVDs). The log-likelihood for the 3D kinematics of the *i*th object is given by

$$\ln L_i = -\frac{1}{2} [\ln(|\mathbf{\Sigma}_i|) + (\mathbf{v}_i - \boldsymbol{\mu})^\mathsf{T} \mathbf{\Sigma}_i^{-1} (\mathbf{v}_i - \boldsymbol{\mu}) + 3 \ln(2\pi)],$$
(4)

where the input kinematic measurement vector for the *i*th object  $v_i$  is defined as

$$\mathbf{v}_i = \begin{bmatrix} v_{\alpha_i} \\ v_{\delta_i} \\ v_{r_i} \end{bmatrix}, \tag{5}$$

while the vectors for the mean velocities and dispersions are defined as

$$\boldsymbol{\mu} = \begin{bmatrix} \bar{v}_{\alpha} \\ \bar{v}_{\delta} \\ \bar{v}_{r} \end{bmatrix}, \qquad \boldsymbol{\sigma} = \begin{bmatrix} \sigma_{v_{\alpha}} \\ \sigma_{v_{\delta}} \\ \sigma_{v_{r}} \end{bmatrix}, \tag{6}$$

and the covariance matrix  $\Sigma_i$  for the *i*th object is defined as

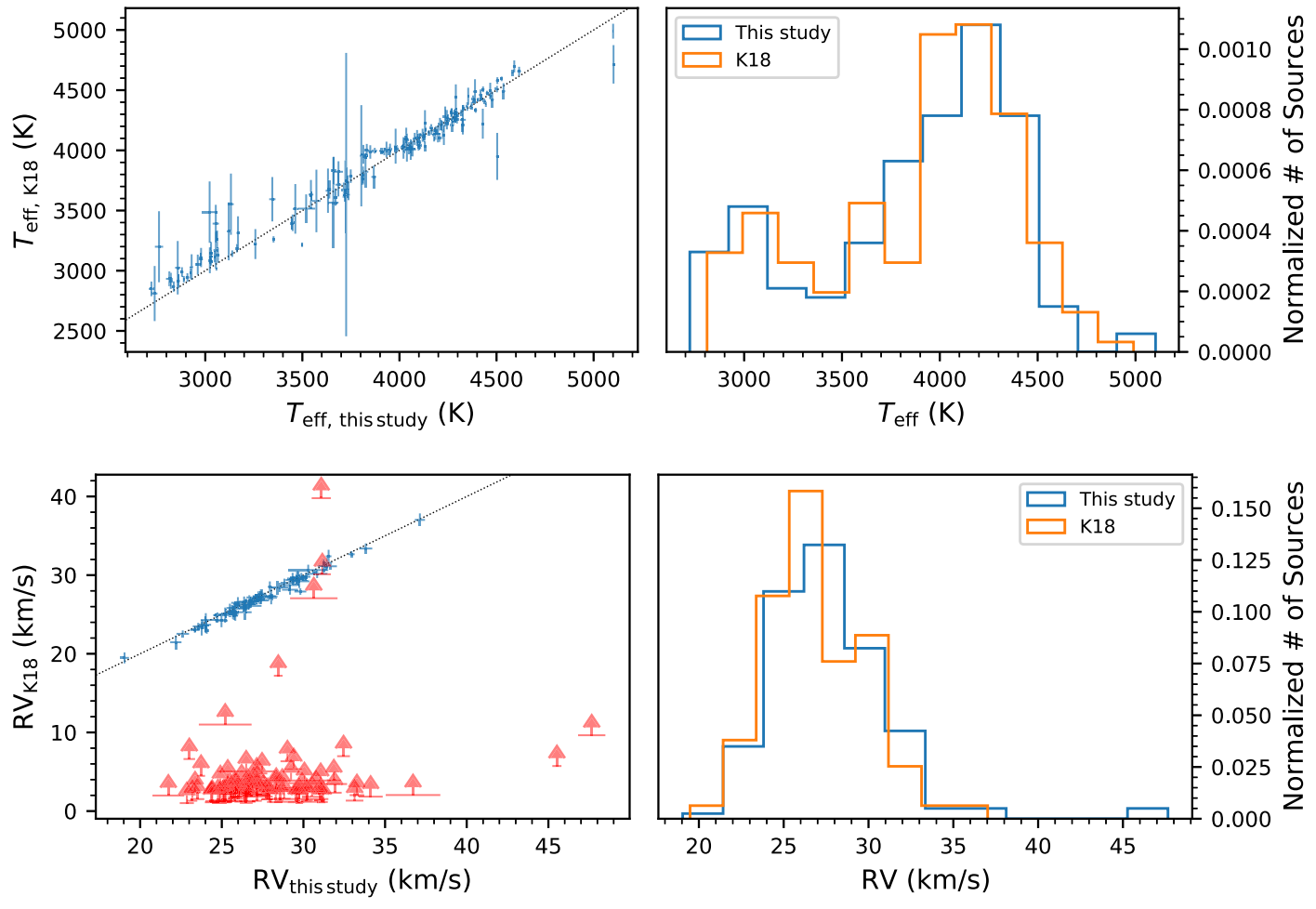


Figure 7. Comparison between our derived parameters using APOGEE spectra and those derived in K18 (168 sources). Black dotted lines indicate where agreement is one-to-one. Top:  $T_{\rm eff}$  comparison. There is a slight offset, with our derived  $T_{\rm eff}$  being slightly lower than that of K18 for  $T_{\rm eff} < 3600$  and slightly higher than K18 for  $T_{\rm eff} > 3600$ . Bottom: RV comparison. Red arrows represent lower limits as reported by K18, while we provide measurements with error bars.

$$\begin{split} & \boldsymbol{\Sigma}_{i} \\ & = \begin{bmatrix} \sigma_{v_{\alpha}}^{2} + \epsilon_{\alpha_{i}}^{2} & \rho_{1}(\sigma_{v_{\alpha}}\sigma_{v_{\delta}} + \epsilon_{\alpha_{i}}\epsilon_{\delta_{i}}) & \rho_{2}(\sigma_{v_{\alpha}}\sigma_{v_{r}} + \epsilon_{\alpha_{i}}\epsilon_{r_{i}}) \\ \rho_{1}(\sigma_{v_{\alpha}}\sigma_{v_{\delta}} + \epsilon_{\alpha_{i}}\epsilon_{\delta_{i}}) & \sigma_{v_{\delta}}^{2} + \epsilon_{\delta_{i}}^{2} & \rho_{3}(\sigma_{v_{\delta}}\sigma_{v_{r}} + \epsilon_{\delta_{i}}\epsilon_{r_{i}}) \\ \rho_{2}(\sigma_{v_{\alpha}}\sigma_{v_{r}} + \epsilon_{\alpha_{i}}\epsilon_{r_{i}}) & \rho_{3}(\sigma_{v_{\delta}}\sigma_{v_{r}} + \epsilon_{\delta_{i}}\epsilon_{r_{i}}) & \sigma_{v_{r}}^{2} + \epsilon_{r_{i}}^{2} \end{bmatrix}. \end{split}$$

The correlation coefficients are given by  $\rho_{1,2,3}$  and should be zero if the covariance is completely uncorrelated. Using Bayes's theorem, for a set of N measurements  $\mathbf{D} \equiv \{\mathbf{v}_i, \, \boldsymbol{\epsilon}_i\}_{i=1}^N$ , the log of the posterior probability is given as

$$\ln P(\boldsymbol{\mu}, \boldsymbol{\sigma}|\boldsymbol{D}) \propto \sum_{i}^{N} [\ln L_{i}(\boldsymbol{v}_{i}, \boldsymbol{\epsilon}_{i}|\boldsymbol{\mu}, \boldsymbol{\sigma}) + \ln p(\boldsymbol{\mu}, \boldsymbol{\sigma})],$$
 (8)

where  $p(\mu, \sigma) \equiv p(\mu)p(\sigma)$  is the prior on the means and dispersions. Similar to Kim et al. (2019), we adopted a flat prior on the mean vector,  $\mu$ , and a Jeffreys prior on the dispersion vector,  $p(\sigma) \propto \sigma^{-1}$ . To determine best-fit parameters for  $\bar{\nu}_{\alpha}$ ,  $\bar{\nu}_{\delta}$ ,  $\bar{\nu}_{r}$ ,  $\sigma_{\nu_{\alpha}}$ ,  $\sigma_{\nu_{\alpha}}$ ,  $\sigma_{\nu_{\gamma}}$ ,  $\rho_{1}$ ,  $\rho_{2}$ , and  $\rho_{3}$ , we utilized the MCMC affine-invariant ensemble sampler *emcee* (Foreman-Mackey et al. 2013).

### 5.3. Kinematic Outliers

Previous studies have identified subpopulations within the ONC with kinematics consistent with high-velocity escaping stars (e.g., Kim et al. 2019; Kuhn et al. 2019; Platais et al. 2020). Kim et al. (2019) and Kuhn et al. (2019) used outliers from an expected normal distribution to determine kinematic outliers. Kim et al. (2019) also used the ONC's 2D mean-square escape velocity ( $\approx$ 3.1 mas yr<sup>-1</sup>, or 6.1 km s<sup>-1</sup> at a distance of 414 pc) to identify potential escaping sources. It should be noted that Kim et al. (2019) used a distance of 414 ± 7 pc from Menten et al. (2007), whereas our adopted value of 388 ± 5 pc would give a mean-square escape velocity of 5.7 km s<sup>-1</sup>. In practice, this should not alter the results, since outliers are computed from the bulk properties of the cluster, and our smaller distance would equally impact all tangential velocities the same.

To determine high-probability escaping or evaporating sources, we identified sources whose velocities deviate from the Gaussian velocity distribution model (see Section 5.2). We used a methodology similar to Kim et al. (2019) and Kuhn et al. (2019), plotting sources on Q-Q plots, where data quantiles ( $Q_{\rm data}$ ) are plotted against theoretical quantiles ( $Q_{\rm theo}$ ) corresponding to a Gaussian distribution. These two quantiles

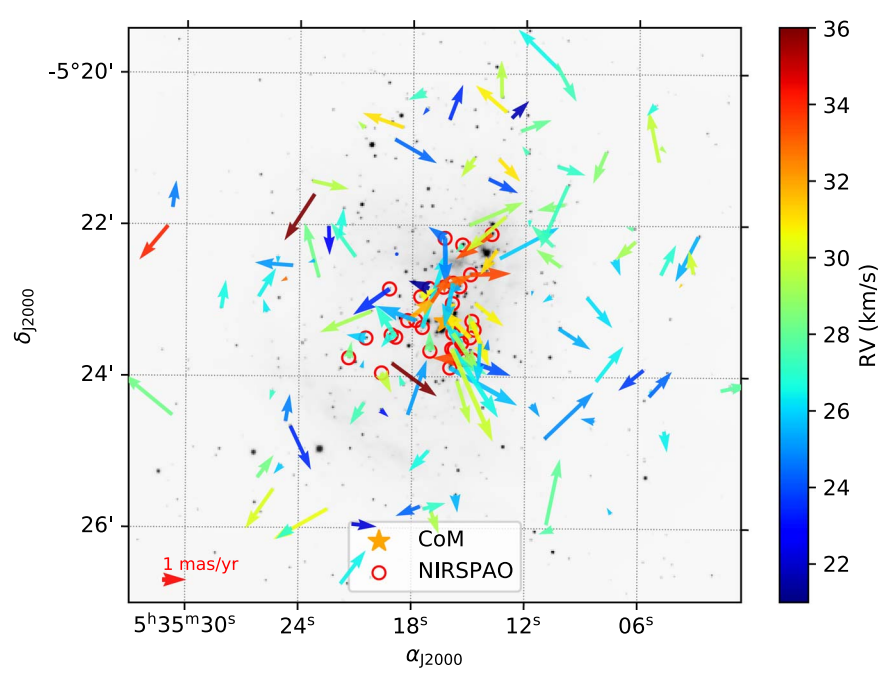


Figure 8. Diagram of PMs and line-of-sight velocities for sources within a  $4' \times 4'$  window centered on the core of the ONC. The background image is a CTIO/Blanco ISPI  $K_s$ -band image from Robberto et al. (2010). Sources with NIRSPAO RVs are denoted with red circles, while the remaining sources have RVs measured from APOGEE data. The CoM for the ONC is indicated by the orange star.

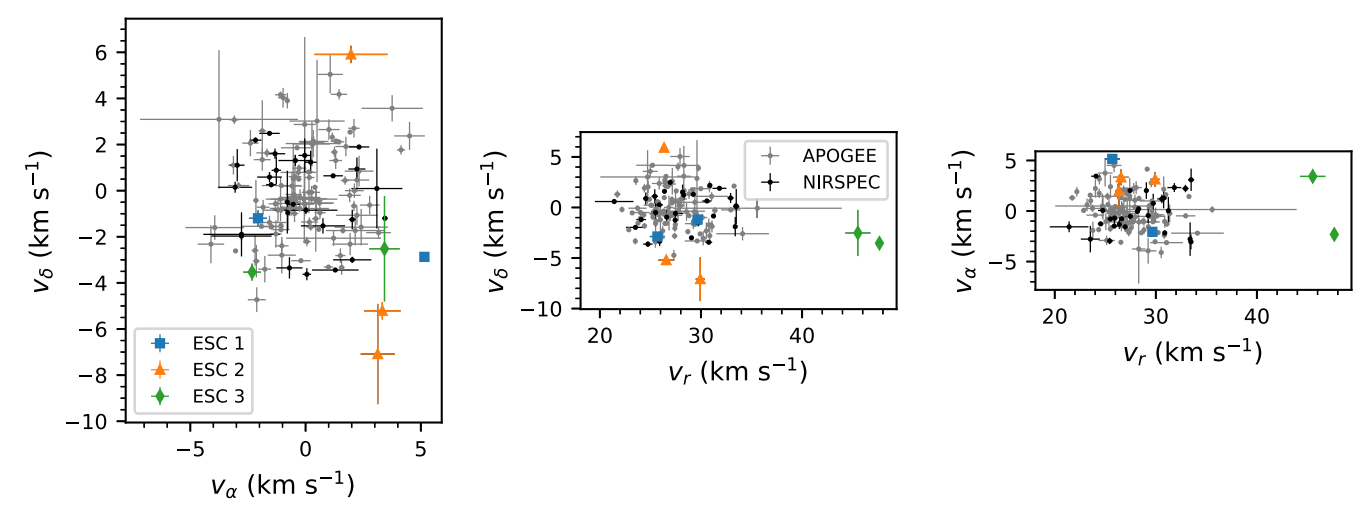


Figure 9. Plots of each velocity component with respect to one another. All axes have equal scaling. Shown are APOGEE measurements (gray points), NIRSPEC measurements (black points), and kinematic outliers (see Section 5.3) from escape groups 1 (blue squares), 2 (orange triangles), and 3 (green diamonds).

are defined as

$$Q_{\text{data},i} = \frac{\nu_{(\alpha,\delta,r)_i} - \bar{\nu}_{(\alpha,\delta,r)}}{\sqrt{\sigma_{(\alpha,\delta,r)}^2 + \epsilon_{(\alpha,\delta,r)_i}^2}},$$
(9)

$$Q_{\text{theo},i} = \sqrt{2} \text{ erf}^{-1} \left( \frac{2(r_i - 0.5)}{n} - 1 \right),$$
 (10)

where  $erf^{-1}$  is the inverse of the error function,  $r_i$  is the rank of the *i*th measurement, and n is the number of measurements.

The means and IVDs are computed using the method outlined in Section 5.2. Figure 10 shows the quantiles for all sources (top panels), quantiles after removing outliers in RV space (middle panels), and quantiles after removing large outliers in RV and tangential kinematic space (bottom panels). In each panel, the gray band indicates the 95% confidence

interval from bootstrapping. Kim et al. (2019) identified two separate groups of kinematic outliers, sources with highly significant deviations within the Q–Q plot ( $Q_{\text{data},X} \geqslant \pm 3$ ; escape group 1) and sources with low-significance escape velocities defined from the angular escape speed (sources with  $\mu_{\text{tot}} > 3.1$  mas yr<sup>-1</sup>; escape group 2). We additionally identify sources with RVs that significantly deviate from the sample ( $Q_{\text{data},Z} \geqslant \pm 3$ ) and label this escape group 3 (see Figures 9 and 10). Kim et al. (2019) and Kuhn et al. (2019) estimated the escape speed for the ONC to be  $\approx$ 6.1 km s<sup>-1</sup> using the virial theorem, and all of the outliers in escape groups 1 and 3 have velocities in excess of this speed. However, it should be noted that velocity outliers in RV space could be potential binaries rather than escaping/evaporating sources.

Of the escaping stars identified in Kim et al. (2019), one of the sources in escape group 1 and three of the sources in escape

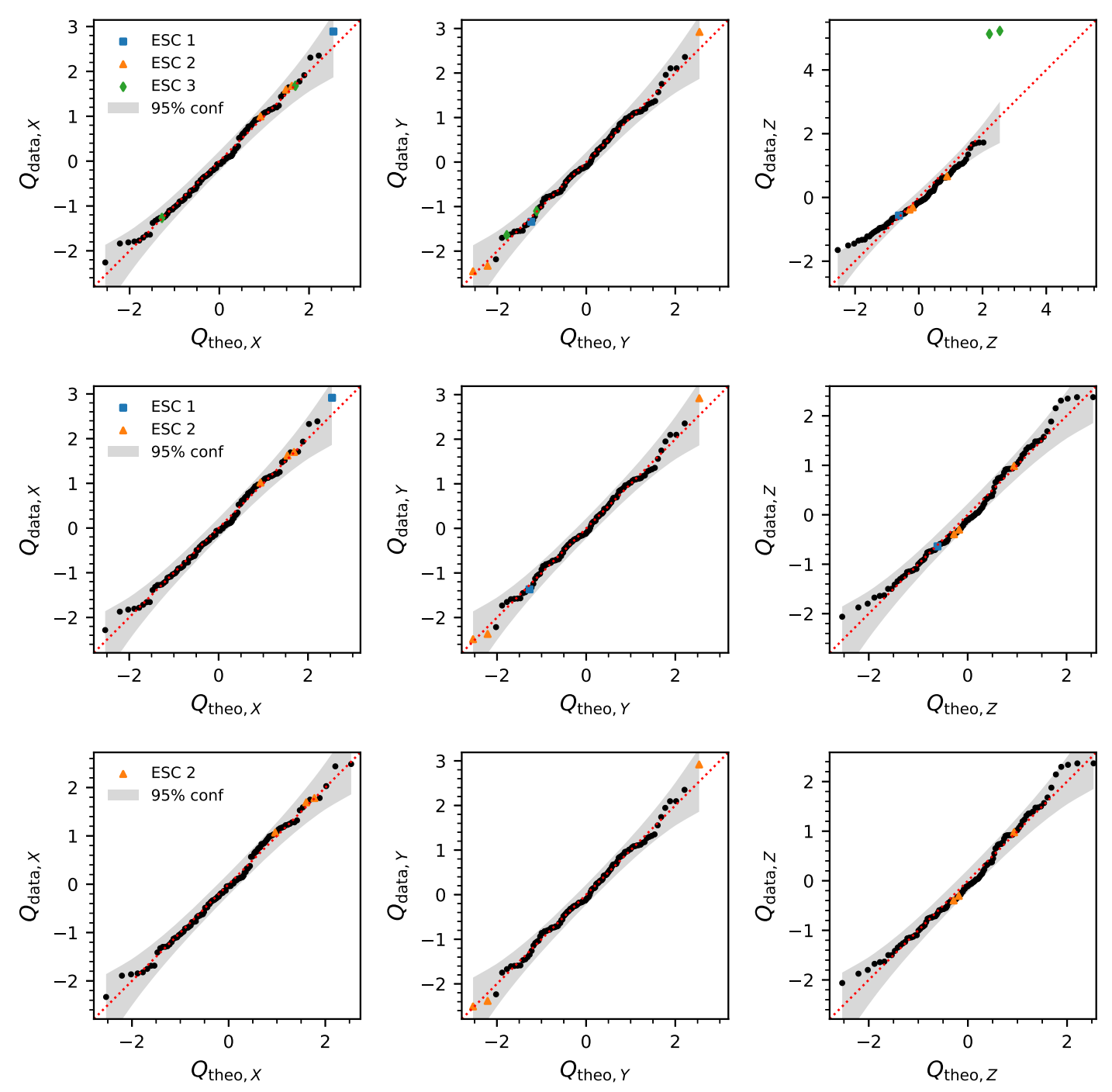


Figure 10. The Q-Q plots showing the normality of the three velocity components (from left to right:  $v_{\alpha}$ ,  $v_{\delta}$ , and  $v_{r}$ ). High-velocity (blue squares) and low-velocity (orange triangles) escaping sources identified by Kim et al. (2019) are indicated. Additionally, velocity outliers from this study are indicated with green diamonds. Top: analysis including all sources. Middle: analysis after removing the escape group 3 sources. Bottom: analysis after removing all sources in escape groups 1 and 3.

group 2 were observed with NIRSPAO, and none were in our reanalyzed APOGEE subsample (identified in Table 3). This is not surprising, as all of the sources in escape groups 1 and 2 are within 2!5 of the ONC CoM (16 of 18 sources within 1'). The majority of sources in escape groups 1 and 2 tend to be fainter (14 of 18 sources with F139 mag  $\gtrsim$ 12) or have a nearby source within 2". All of the sources in escape groups 1 and 2 have RVs that are consistent with the bulk RV distribution of the ONC. Conversely, none of the sources in escape group 3 (line-of-sight velocity outliers) are within escape groups 1 and 2, and

both escape group 3 sources are APOGEE sources. This indicates that the high-velocity components for these sources are primarily in either the tangential or line-of-sight direction, but not both.

### 5.4. Intrinsic Velocity Dispersions

Using the framework outlined in Section 5.2, we computed intrinsic velocity dispersions (IVDs) after removing all sources in escape groups 1 and 3. The values from our model were

Table 3 NIRSPEC Forward-modeling Results

(HC 2000)	ID <sup>a</sup>	$\alpha_{\rm J2000}$	$\delta_{ m J2000}$	$\overline{RV}^{\mathbf{b}}$	$\mu_{\alpha\cos\delta}$	$\mu_\delta$	$T_{\mathrm{eff}}^{}\mathrm{c}}$	v sin i	$\left(F_{\text{O33,cont}}\right)$	Note <sup>e</sup>
		(deg)	(deg)	$(km s^{-1})$	(mas yr <sup>-1</sup> )	(mas yr <sup>-1</sup> )	(K)	$(km s^{-1})$	$\left(\frac{F_{\text{O33,*}}}{F_{\text{O33,*}}}\right)$	
135		83.80950000	-5.40686111	$28.56 \pm 0.91$	•••		$3610 \pm 300$	$49.33 \pm 2.26$	0.24	
188	559	83.83175000	-5.39925000	$29.74\pm0.27$	$0.41\pm0.52$	$-0.83 \pm 0.18$	$3475\pm73$	$6.90 \pm 1.72$	0.01	
202	615	83.81666667	-5.39805556	$25.69 \pm 0.75$	$2.80\pm0.06$	$-1.56 \pm 0.08$	$3393 \pm 204$	$42.27 \pm 2.95$	0.75	E1
204		83.84087500	-5.39830556	$24.73 \pm 0.55$		•••	$3712\pm50$	$48.16 \pm 2.56$	0.28	
215		83.80116667	-5.39669444	$27.91 \pm 0.27$	•••	•••	$3641\pm33$	$9.03 \pm 1.41$	0.20	
217		83.83770833	-5.39694444	$29.73 \pm 0.35$	•••	•••	$3614 \pm 33$	$47.35 \pm 0.89$	0.23	V
219	87	83.81316667	-5.39630556	$24.08 \pm 0.48$	$1.87 \pm 0.06$	$-0.65 \pm 0.02$	$3486\pm57$	$20.78 \pm 1.40$	0.43	
220	23	83.81175000	-5.39625000	$33.47\pm0.23$	$-1.66 \pm 0.40$	$0.08\pm0.13$	$3484 \pm 19$	$9.04\pm0.30$	0.02	
223	164	83.81433333	-5.39597222	$27.45 \pm 0.23$	$1.10 \pm 0.08$	$-0.68 \pm 0.23$	$3359 \pm 16$	$9.74 \pm 0.69$	0.32	
224	•••	83.79475000	-5.39575000	$25.94 \pm 0.15$		•••	$3859 \pm 21$	$24.94 \pm 0.58$	0.00	
228	•••	83.80250000	-5.39561111	$27.46 \pm 0.27$		•••	$3782 \pm 30$	$40.37 \pm 0.78$	0.46	
229	536	83.83904167	-5.39594444	$28.30 \pm 0.21$	$0.12 \pm 0.14$	$0.67 \pm 0.27$	$3613 \pm 79$	$12.19 \pm 1.21$	0.15	
240	•••	83.80604167	-5.39455556	$27.11 \pm 0.44$			$3640 \pm 65$	$14.15 \pm 1.28$	3.89	
244	180	83.82108333	-5.39438889	$28.18 \pm 0.11$	$-0.02 \pm 0.15$	$0.83 \pm 0.40$	$3436 \pm 17$	$21.29 \pm 0.83$	0.04	
245	•••	83.81229167	-5.39425000	$31.05 \pm 0.21$	•••		$3869 \pm 18$	$17.03 \pm 0.35$	0.00	
248	200	83.81566667	-5.39400000	$26.56 \pm 0.78$	$1.81 \pm 0.43$	$-2.83 \pm 0.20$	$3438 \pm 48$	$39.39 \pm 3.82$	0.35	E2
250	197	83.81625000	-5.39388889	$29.93 \pm 0.46$	$1.70 \pm 0.40$	$-3.85 \pm 1.18$	$2975 \pm 91$	$15.90 \pm 1.86$	0.39	E2
253	•••	83.82587500	-5.39330556	$28.67 \pm 0.36$	•••	•••	$4000 \pm 117$	$6.21 \pm 1.48$	2.66	
258	521	83.81000000	-5.39269444	$28.02 \pm 0.19$	$-0.11 \pm 0.23$	$-1.65 \pm 0.03$	$3568 \pm 41$	$7.71 \pm 1.03$	0.82	
259	•••	83.82112500	-5.39277778	$27.53 \pm 0.08$	•••		$3501 \pm 44$	$32.49 \pm 1.95$	0.54	
261	206	83.81408333	-5.39261111	$26.39 \pm 0.20$	$-0.72 \pm 0.24$	$0.87 \pm 0.12$	$3374 \pm 14$	$1.49 \pm 0.31$	0.00	
275	65	83.81220833	-5.39141667	$30.88 \pm 0.01$	$-1.18 \pm 0.14$	$1.19 \pm 0.06$	$3860 \pm 17$	$17.59 \pm 0.30$	0.00	
277A	530	83.83525000	-5.39158333	$25.88 \pm 0.36$	$-0.81 \pm 0.12$	$0.14 \pm 0.06$	$3444 \pm 51$	$12.90 \pm 2.65$	0.36	В
282	44	83.82866667	-5.39136111	$26.96 \pm 0.28$	$-0.85 \pm 0.24$	$1.35 \pm 0.03$	$3394 \pm 22$	$5.59 \pm 1.05$	1.06	
288	71	83.82966667	-5.39086111	$26.61 \pm 0.17$	$-0.42 \pm 0.04$	$-0.52 \pm 0.41$	$3666 \pm 54$	$18.20 \pm 0.53$	0.25	
291	211	83.81600000	-5.39044444	$29.06 \pm 0.22$	$1.10 \pm 0.45$	$-1.63 \pm 0.07$	$3181 \pm 33$	$15.83 \pm 0.72$	0.42	В
295	•••	83.82320833	-5.39025000	$21.85 \pm 0.93$	•••	•••	$3662 \pm 305$	$22.69 \pm 7.18$	0.76	
302	221	83.81133333	-5.38969444	$29.24 \pm 0.11$	$-0.24 \pm 0.40$	$0.71 \pm 0.13$	$3541 \pm 21$	$13.73 \pm 1.12$	0.48	
306A	•••	83.81600000	-5.38958333	$29.12 \pm 0.50$	•••	•••	$4201 \pm 229$	$25.92 \pm 1.36$	1.12	В
306B	•••	83.81600000	-5.38958333	$21.15 \pm 0.54$	•••	•••	$3473 \pm 35$	$40.15 \pm 2.53$	0.64	В
313	198	83.82279167	-5.38919444	$26.35 \pm 0.19$	$1.07 \pm 0.86$	$3.21 \pm 0.20$	$4206 \pm 235$	$10.04 \pm 0.93$	0.64	E2
322	•••	83.81787500	-5.38794444	$24.90 \pm 0.27$	•••	•••	$3414 \pm 18$	$37.47 \pm 0.92$	0.07	
324	226	83.81183333	-5.38777778	$30.77 \pm 0.34$	$0.70 \pm 0.55$	$-1.87 \pm 0.04$	$3449 \pm 36$	$5.12 \pm 1.21$	0.01	
331	121	83.82604167	-5.38769444	$31.83 \pm 0.69$	$1.26 \pm 0.24$	$1.03 \pm 0.04$	$4034 \pm 452$	$18.92 \pm 1.17$	0.64	
332A	183	83.82425000	-5.38766667	$25.43 \pm 0.32$	$-1.61 \pm 0.17$	$0.60 \pm 0.38$	$4012 \pm 37$	$16.48 \pm 0.43$	0.01	BC
370	227	83.81616667	-5.38388889	$31.24 \pm 0.17$	$0.01 \pm 0.74$	$-0.46 \pm 0.09$	$3802 \pm 45$	$14.43 \pm 0.34$	0.66	
375	560	83.82075000	-5.38361111	$33.19 \pm 0.45$	$0.78 \pm 0.13$	$1.15 \pm 0.04$	$4225 \pm 244$	$26.95 \pm 0.70$	0.41	
386		83.81362500	-5.38241667	$27.44 \pm 0.18$			$3673 \pm 13$	$11.20 \pm 0.10$	0.11	
388	532	83.82316667	-5.38244444	$30.59 \pm 0.46$	$0.65\pm0.23$	$0.35 \pm 0.04$	$4279 \pm 142$	$17.83 \pm 1.46$	0.52	
389		83.81516667	-5.38233333	$30.86 \pm 0.15$			$3566 \pm 34$	$26.89 \pm 0.46$	0.68	
408	143	83.83008333	-5.38075000	$23.52 \pm 0.94$	$-1.51 \pm 0.71$	$-1.07 \pm 0.10$	$3660 \pm 105$	$50.79 \pm 1.85$	0.02	
410	62	83.82133333	-5.38058333	$21.42 \pm 1.91$	$-0.85 \pm 0.29$	$0.32 \pm 0.12$	$3910 \pm 94$	$57.77 \pm 2.25$	0.03	
412	151	83.81808333	-5.38030556	$32.93 \pm 0.32$	$1.21 \pm 0.20$	$0.51 \pm 0.27$	$3563 \pm 28$	$31.96 \pm 1.61$	0.80	
413	35	83.81454167	-5.38016667	$25.51 \pm 0.41$	$-0.43 \pm 0.04$	$-0.27 \pm 0.74$	$3643 \pm 44$	$28.79 \pm 0.55$	0.05	
420	154	83.81600000	-5.37941667	$25.91 \pm 0.24$	$-0.38 \pm 0.31$	$-1.82 \pm 0.25$	$3510 \pm 35$	$24.16 \pm 0.67$	0.00	
425		83.82479167	-5.37930556	$24.94 \pm 0.25$			$3576 \pm 22$	$21.83 \pm 0.32$	0.00	
431	700	83.81216667	-5.37752778	$33.49 \pm 0.31$	$1.68 \pm 0.60$	$0.05 \pm 0.94$	$3603 \pm 22$	$18.80 \pm 0.97$	0.65	
436	•••	83.82658333	-5.37708333	$32.93 \pm 0.08$	•••	•••	$3658 \pm 347$	$16.30 \pm 0.90$	0.11	
440	•••	83.82233333	-5.37661111	$28.52 \pm 0.48$	•••	•••	$3715 \pm 88$	$23.57 \pm 1.07$	1.37	
450		83.82087500	-5.37586111 5.37100000	$26.23 \pm 0.24$			$3674 \pm 54$	$12.14 \pm 0.74$	0.02	
504	64	83.81395833	-5.37100000	$27.48 \pm 0.78$	$-0.29 \pm 0.15$	$-0.32 \pm 0.02$	$3969 \pm 295$	$30.65 \pm 1.86$	3.79	
522A	110	83.81787500	-5.36955556	$24.75 \pm 0.47$	$0.03 \pm 0.10$	$-1.97 \pm 0.14$	$3441 \pm 24$	$33.48 \pm 1.98$	0.31	В
522B	642	83.81787500	-5.36955556	$24.54 \pm 0.28$	$-0.69 \pm 0.11$	$0.48 \pm 0.33$	$3170 \pm 39$	$21.94 \pm 1.20$	0.80	В
546	567	83.81250000	-5.36666667	$21.51 \pm 0.18$	$2.25 \pm 0.09$	$0.96 \pm 0.11$	$3793 \pm 56$	$15.32 \pm 1.18$	0.27	V
703	137	83.80750000	-5.36863889	$33.39 \pm 0.06$	$-1.51 \pm 0.90$	$-1.03 \pm 0.52$	$3584 \pm 27$	$9.14 \pm 0.41$	1.24	
713	• • • •	83.82795833	-5.38247222	$22.95 \pm 0.31$	•••	•••	$4988 \pm 192$	$6.75 \pm 1.54$	1.60	

(This table is available in machine-readable form.)

b Reported uncertainties also include the  $0.058~{\rm km~s^{-1}}$  systematic uncertainty between calibration frames and the 0.5% variation found from differing  $\log g$  and  $T_{\rm eff}$ . Continuum veiling causes extreme degeneracies with  $T_{\rm eff}$ . Caution should be taken when using derived temperatures with high veiling.

<sup>&</sup>lt;sup>d</sup> Order 33 veiling parameter.

e In this column, B = double star, previously known in the literature (Hillenbrand 1997; Robberto et al. 2013); BC = new binary candidates, previously reported as single in the literature; E1 = escape group 1; E2 = escape group 2; V = RV variable source.

$$\begin{split} \bar{v}_{\alpha} &= 0.01 \, \pm \, 0.16 \, \, \mathrm{km \, s^{-1}}, \\ \bar{v}_{\delta} &= -0.09 \, \pm \, 0.18 \, \, \mathrm{km \, s^{-1}}, \\ \bar{v}_{r} &= 27.45^{+0.21}_{-0.22} \, \, \mathrm{km \, s^{-1}}, \\ \sigma_{v_{\alpha}} &= 1.64 \, \pm \, 0.12 \, \, \mathrm{km \, s^{-1}}, \\ \sigma_{v_{\delta}} &= 2.03 \, \pm \, 0.13 \, \, \mathrm{km \, s^{-1}}, \\ \sigma_{v_{r}} &= 2.56^{+0.16}_{-0.17} \, \, \mathrm{km \, s^{-1}}, \\ \rho_{1} &= 0.06 \, \pm \, 0.09, \\ \rho_{2} &= -0.11 \, \pm \, 0.09, \\ \rho_{3} &= -0.05 \, \pm \, 0.09. \end{split}$$

The correlation coefficients are consistent with zero, indicating little to no correlation between velocity components.

Our computed velocity dispersions are roughly consistent with other studies in both the tangential (plane of the sky) direction,  $(\sigma_{v_n}, \sigma_{v_b}) = (1.63 \pm 0.04, 2.20 \pm 0.06) \, \mathrm{km \ s^{-1}}$  (K19),  $(\sigma_{v_n}, \sigma_{v_b}) = (1.85 \pm 0.04, 2.45 \pm 0.06) \, \mathrm{km \ s^{-1}}$  (Platais et al. 2020), and  $(\sigma_{v_n}, \sigma_{v_b}) = (1.79 \pm 0.12, 2.32 \pm 0.10) \, \mathrm{km \ s^{-1}}$  (Jones & Walker 1988), and in the line-of-sight direction,  $\sigma_{v_r} \approx 3.1 \, \mathrm{km \ s^{-1}}$  (Fűrész et al. 2008),  $\sigma_{v_r} \approx 2.1 - 2.4 \, \mathrm{km \ s^{-1}}$  (Tobin et al. 2009), and  $\sigma_{v_r} \approx 2.2 \, \mathrm{km \ s^{-1}}$  (Da Rio et al. 2017). However, our derived value of  $\sigma_{v_r} = 2.56^{+0.16}_{-0.17} \, \mathrm{km \ s^{-1}}$  is slightly higher than the value measured in Tobin et al. (2009) and Da Rio et al. (2017). This is possibly due to our closer proximity to the ONC core than previous studies or potentially the target selection of fainter, redder (lower-mass) sources. This may also indicate kinematic structure along the line-of-sight direction, similar to the velocity elongation seen in the north–south direction along the filament (e.g., Jones & Walker 1988). It is also possible that this component potentially suffers from the impact of unresolved binaries, which we evaluate in the next section.

We identified one new binary candidate within our sample ([HC 2000] 332A), along with six other targets that are components of apparent doubles (candidate binaries). At least one source ([HC 2000] 546) shows significant RV variability between the APOGEE and NIRSPAO measurements, although no secondary component was detected in the AO imaging. There is only one epoch of APOGEE data and one epoch of NIRSPAO data for [HC 2000] 546; therefore, it is not possible to determine the orbital parameters of this potential binary without additional observations. Two of our sources have multiepoch NIRSPAO observations ([HC 2000] 229 and [HC 2000] 217); however, the RVs computed at each epoch are consistent with one another within the errors.

### 5.4.1. Unresolved Binarity

The RVs are instantaneous velocity measurements, in contrast to PM measurements, which are taken over baselines of years. The effects of binary orbital motion therefore influence RV measurements but are typically averaged out over the long time baselines of PM measurements. Consequently, it is important for us to quantify the potential effects that unresolved binaries may have on the line-of-sight velocity dispersion(s).

Raghavan et al. (2010) did an extensive multiplicity study of solar-type stars, both in the field and young sources determined from chromospheric activity. Their findings were that the overall field multiplicity of solar-type stars is  $44\% \pm 4\%$ , with the multiplicity fraction of younger sources being statistically equivalent  $40\% \pm 3\%$ . Additionally, Raghavan et al. (2010) also noted a declining trend in the multiplicity fraction with

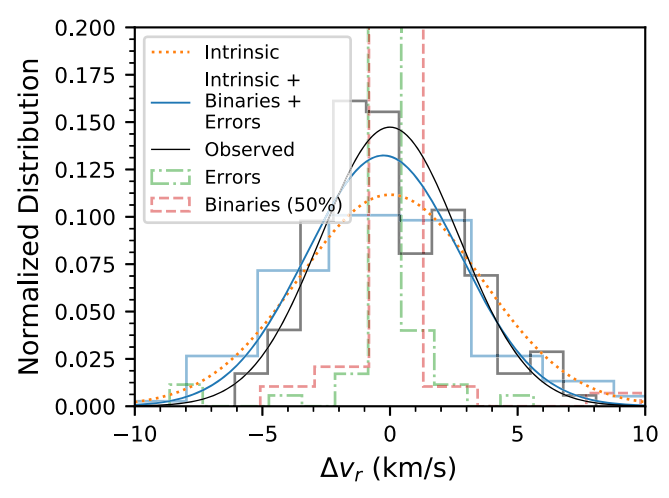


**Figure 11.** Example of a single model generated in our binary simulation. The gray distribution and black solid line indicate our observations. The orange dotted line shows the intrinsic IVD distribution, and the green dashed—dotted and red dashed lines indicate the distributions of uncertainties and binaries, respectively. The blue line and distribution show the final distribution accounting for binaries and uncertainties, which is compared to observations. Binaries and measurement uncertainties work to widen the dispersion, making the observed velocity dispersion larger than the IVD.

redder color (lower primary mass). Down to the M dwarf regime, the multiplicity fraction for the field is estimated to be  $\sim$ 20%–25%, declining with lower primary mass (Fischer & Marcy 1992; Clark et al. 2012; Ward-Duong et al. 2015; Bardalez Gagliuffi et al. 2019).

In the ONC, estimates of visual binaries range from  $\sim 3\%$ –30% (Köhler et al. 2006; Reipurth et al. 2007; Duchêne et al. 2018; De Furio et al. 2019; Jerabkova et al. 2019). Over the specific range investigated by Duchêne et al. (2018)—0.3–2  $M_{\odot}$  with companions within 10–60 au—they found the ONC binary fraction to be approximately 10% higher than the field population estimates from Raghavan et al. (2010) and Ward-Duong et al. (2015). Combined, this would place the binary fraction between 30% and 50% for systems with primary masses between 0.1 and  $1M_{\odot}$ . These results are roughly consistent with modeling estimates (e.g., Kroupa et al. 1999; Kroupa 2000; Kroupa et al. 2001).

With such a large potential binary fraction in the ONC, it is important to quantify how orbital motion can affect our measured line-of-sight velocity dispersion. This is primarily important to determine whether the observed anisotropy between the line-of-sight component and the tangential components is explained with orbital motion, or if there is a true elongation along the line-of-sight velocities.

### 5.4.2. Simulating the Effect of Binaries

To determine the effects of unresolved binarity on the IVD, we performed a test similar to Da Rio et al. (2017) and Karnath et al. (2019). First, we generate a random intrinsic dispersion drawn from a uniform sample between 1 and 4 km s<sup>-1</sup>. Next, we convolve this dispersion with the measurement error distribution. We use our observed measurement error distribution from the APOGEE+NIRSPEC data set and create an inverse cumulative distribution function, which we randomly sample to build the error distribution. Lastly, we convolve this distribution with a velocity distribution from a set of synthetic binaries and compare the final distribution to our observed distribution.

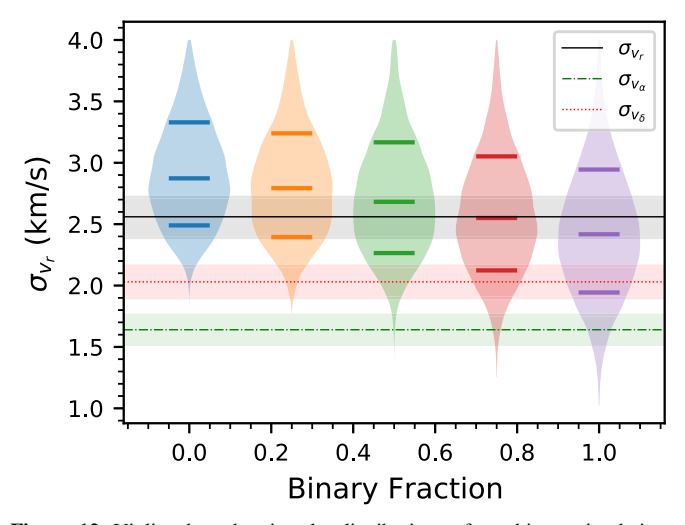


Figure 12. Violin plots showing the distributions of our binary simulations. Distributions are generated at binary fractions of 0%, 25%, 50%, 75%, and 100%, and lines within each distribution indicate 16th, 50th, and 84th percentiles. Our measured IVD (black line and gray  $1\sigma$  confidence region) is consistent with essentially all binary fractions. We also show our tangential IVD components in  $\alpha$  (green dotted–dashed line and region) and  $\delta$  (red dotted line and region), indicating that the binary fraction would need to be  $\gtrsim\!75\%$  to bring the line-of-sight component within the range of the tangential components.

To generate our synthetic systems, we first generate a distribution of stars with masses between 0.1 and  $1\,M_\odot$ . We apply a binary fraction (discussed below) to our sample and use the mass ratio distribution from Reggiani & Meyer (2013) to determine component masses within each system. Next, for binary systems, we apply the eccentricity distribution from Duchêne & Kraus (2013) and the period distribution from Raghavan et al. (2010).

For our simulations, we generate 135 systems (the same number of sources in our 3D kinematics sample). These synthetic systems are created using the velbin package (Cottaar & Hénault-Brunet 2014; Foster et al. 2015). This sampling assumes random orbits with random orientations and provides a 1D RV distribution.

This distribution is then compared to our observed APOGEE +NIRSPEC RV distribution, requiring that the standard deviation of the synthetic distribution be within  $2\sigma$  of the observed distribution's standard deviation. An example of one randomly drawn distribution compared to our observed distribution is shown in Figure 11. The binary contribution to the resulting distribution is typically far less than the intrinsic dispersion and measurement error distribution, a result also noted by Da Rio et al. (2017).

We kept the first  $10^5$  models that fit our similarity criteria stated above and generated a distribution of IVDs that passed the similarity criteria of our observed RV distribution. We performed this test for binary fractions of 0%, 25%, 50%, 75%, and 100%. Figure 12 shows our simulation results compared to our IVD determined in Section 5.4. Figure 12 illustrates that our measured IVD is consistent with any level of binarity; however, for the line-of-sight component to be consistent with the tangential components, the ONC would need a binary fraction  $\gtrsim 75\%$ , which is inconsistent with observations and modeling results. Therefore, the larger measured  $\sigma_{\nu_r}$  is likely due to formation/evolution rather than binary effects, and the apparent elongation in the line-of-sight component appears to be real rather than a systematic.

### 6. Discussion

### 6.1. Virial State of the ONC Core

A number of studies have examined whether the ONC is virialized (e.g., Jones & Walker 1988; Da Rio et al. 2014, 2017; Kim et al. 2019; Kuhn et al. 2019). Da Rio et al. (2014) estimated a 1D mean velocity dispersion of  $\sigma_{\nu,1D}\approx 1.73~{\rm km~s^{-1}}$  if the ONC is in virial equilibrium. To test for a virialized state, we adopt a methodology similar to Kim et al. (2019), computing the 1D velocity dispersion as a function of radial distance outward.

To balance the small numbers in our sample, we chose radial bins of size 1'. For each bin, we computed the velocity dispersion using the methods outlined in Section 5.2. The values of  $\sigma_{\alpha}$  and  $\sigma_{\delta}$  were then used to compute the 1D velocity dispersion, i.e.,  $\sigma_{\nu,1D}^2 = (\sigma_{\nu_{\alpha}}^2 + \sigma_{\nu_{\delta}}^2)/2$ . Our computed velocity dispersions are listed in Table 4 and plotted in Figure 13. We also show the 1D velocity dispersion predicted for models of virial equilibrium using the estimated combined gas and stellar mass from Da Rio et al. (2014, solid line). We assigned a 30% mass uncertainty, similar to Kim et al. (2019), which is illustrated with dotted lines. It should be noted that the model from Da Rio et al. (2014) assumes a spherical potential; however, there is evidence that the potential is closer to an elongated spheroid (e.g., Hillenbrand & Hartmann 1998; Carpenter 2000; Kuhn et al. 2014; Kuznetsova et al. 2015; Megeath et al. 2016).

The 1D velocity dispersion computed from PMs is extremely consistent with the results of Kim et al. (2019), which is expected because our subsample originated from their catalog. The 1D velocity dispersions favor a virialized state for the majority of the ONC. The radial distribution of  $\sigma_{v_r}$  is similar to that from Da Rio et al. (2017, see Figure 12 therein) for the ONC, although they only showed one bin from  $R \sim 0$ –0.4 pc. However, they also found a dispersion  $1\sigma$  higher than the virial equilibrium model predicts. We also computed the 1D velocity dispersion using all three velocity components,  $\sigma_{\nu,1\mathrm{D}_{3\mathrm{D}}}^2 = (\sigma_{\nu_{\alpha}}^2 + \sigma_{\nu_{\delta}}^2 + \sigma_{\nu_{r}}^2)/3$ , listed in Table 4. This measurement marginalizes over potential differences in a single velocity component. Figure 13 (bottom panel) shows that only the bin closest to the ONC core appears elevated from the virialized model; however, this method may wash out features in a single velocity component that deviate from a virialized state. These results add to the growing evidence that the core of the ONC is not fully virialized. Additionally, we do not find evidence of global expansion similar to the results of Kim et al. (2019). Without accurate distances to individual sources, we are not able to explore whether there is expansion along the line-of-sight velocity component.

### 6.2. Effects from the Integral-shaped Filament

The Trapezium sits approximately in the middle of the "integral-shaped filament" (ISF; Bally et al. 1987), a long filament of gas with an approximate "S" shape, and 0.1–0.3 pc in front of the filament (e.g., Baldwin et al. 1991; Wen & O'dell 1995; O'Dell 2018; Abel et al. 2019). There has been an observed elongation in the line-of-sight velocity component, which Stutz & Gould (2016) attributed to interactions with the ISF using APOGEE data. The mechanism put forth by Stutz & Gould (2016) to explain the observed elongation in velocity space is the "slingshot" mechanism, where stars born along the filament could be ejected due to the filament undergoing transverse acceleration while the protostar continually accretes

 Table 4

 Velocity Dispersions as a Function of Distance

Radii (arcmin)	$(\operatorname{km}^{\sigma_{\nu_{\alpha}}} \operatorname{s}^{-1})$	$(\operatorname{km}^{\sigma_{\nu_{\delta}}})^{-1}$	$(\text{km s}^{-1})$	$(\operatorname{km} \operatorname{s}^{-1})$	$(\text{km s}^{-1})$	$(\operatorname{km} \operatorname{s}^{-1})$	$(\text{km s}^{\sigma_{\nu,1\text{D}_{3\text{D}}}})$	N
0–1	$1.98^{+0.27}_{-0.27}$	$2.55^{+0.31}_{-0.31}$	$2.22^{+0.29}_{-0.29}$	$2.38^{+0.31}_{-0.31}$	$2.28^{+0.21}_{-0.29}$	$3.17^{+0.39}_{-0.39}$	$2.61^{+0.25}_{-0.31}$	30
1–2	$1.71^{+0.23}_{-0.23}$	$1.95^{+0.24}_{-0.24}$	$1.46^{+0.19}_{-0.19}$	$2.12^{+0.26}_{-0.26}$	$1.84^{+0.16}_{-0.21}$	$2.41^{+0.28}_{-0.28}$	$2.04^{+0.18}_{-0.23}$	32
2-3	$1.74^{+0.19}_{-0.19}$	$1.86^{+0.21}_{-0.21}$	$1.77^{+0.20}_{-0.20}$	$1.85^{+0.20}_{-0.20}$	$1.80^{+0.14}_{-0.17}$	$2.56^{+0.29}_{-0.29}$	$2.08^{+0.17}_{-0.20}$	42
3–4	$1.45^{+0.22}_{-0.22}$	$2.22^{+0.33}_{-0.33}$	$1.88^{+0.29}_{-0.29}$	$1.94^{+0.27}_{-0.27}$	$1.87^{+0.21}_{-0.29}$	$1.92^{+0.30}_{-0.30}$	$1.89^{+0.21}_{-0.28}$	22

mass. The reason for the ejection is that "when the protostar system becomes sufficiently massive to decouple from the filament, it is released" (Stutz & Gould 2016). Such a mechanism would provide an additional contribution to a larger velocity dispersion. However, the slingshot mechanism is dependent on the direction of the transverse acceleration of the filament (i.e., along the line of sight or tangential on the plane of the sky). As the filament runs north–south in the region of the Trapezium, this could provide the mechanism for the observed anisotropy in the tangential velocity components, as well as the radial component. This could be an important effect, as Stutz & Gould (2016) found that the gravity of the background filament likely dominates the gravity field from the stars

From the analysis of Stutz & Gould (2016), the region we have analyzed here contains primarily stars versus protostars, determined based on their excess IR emission. However, Stutz & Gould (2016) only considered the radial component of motion and not the tangential components. Additionally, their RV sources were obtained from APOGEE, providing very few sources within the central 0.1 pc of the core region where we observe the highest velocity dispersion along the line of sight. As such, there is additional work to determine how the ISF might work to influence the measured velocity dispersions. Although we do not provide an in-depth theoretical analysis here to compare to observational data, one is warranted.

### 6.3. Velocity Isotropy

There is a known kinematic anisotropy in the tangential velocities along the north–south direction (e.g., McNamara 1976; Hillenbrand & Hartmann 1998; Da Rio et al. 2014; Kim et al. 2019). However, the deviation from tangential to radial (i.e., toward the center of the cluster) anisotropy ( $\sigma_{tan}/\sigma_{rad}-1$ ; Bellini et al. 2018) of  $0.03\pm0.04$  found by Kim et al. (2019) is consistent with isotropic velocities in the tangential–radial velocity space. It should be noted that throughout this section, we use "radial" ( $\nu_{rad}$ ) to indicate motion on the plane of the sky pointing toward the cluster center, "tangential" ( $\nu_{tan}$ ) to indicate motion on the plane of the sky that is tangential to the previously mentioned radial component, and "line-of-sight" ( $\nu_r$ ) to indicate the RV component of motion.

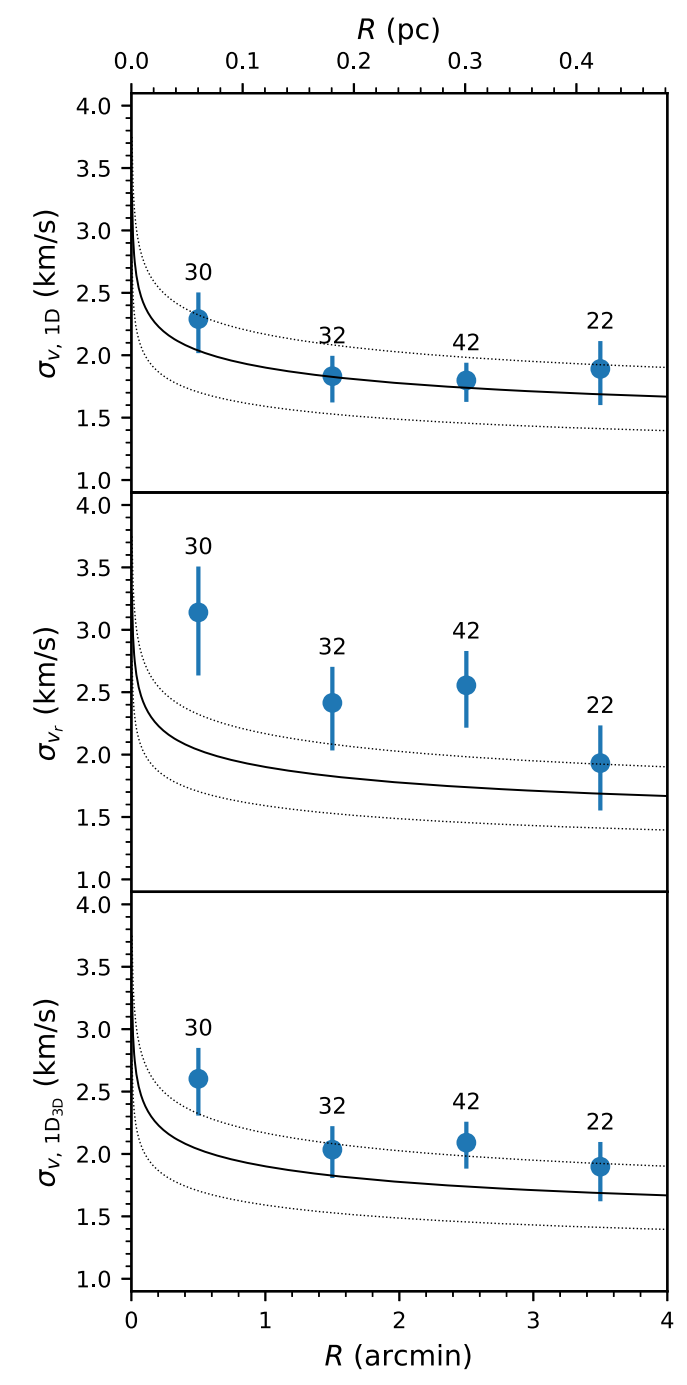
With our 3D kinematic information, we can now compute the ratio of the tangential dispersion to the line-of-sight dispersion  $(\sigma_{\nu_{\rm 1D}}/\sigma_{\nu_{\rm r}})$ . Figure 14 shows the velocity ratios for  $\sigma_{\nu_{\alpha}}/\sigma_{\nu_{\delta}}$  (top) and  $\sigma_{\nu_{\rm 1D}}/\sigma_{\nu_{\rm r}}$  (bottom). The  $\sigma_{\nu_{\alpha}}/\sigma_{\nu_{\delta}}$  shows a north–south elongation, which is consistent with previous studies, e.g.,  $\sigma_{\mu_{\alpha\cos\delta}}/\sigma_{\mu_{\delta}}=0.74\pm0.03$  (Kim et al. 2019) and  $b/a\approx0.7$  (Da Rio et al. 2014); see also Jones & Walker (1988) and Kuhn et al. (2019).

We also decomposed tangential velocities to radial ( $v_{rad}$ ) and tangential ( $v_{tan}$ ) coordinates, both on the plane of the sky, through a change of basis where the radial axis points toward the ONC

CoM. We note that both of these components,  $v_{\rm rad}$  and  $v_{\rm tan}$ , are strictly on the plane of the sky and do not include any line-of-sight velocity components within their vectors. The ratio of  $\sigma_{v_{\rm rad}}/\sigma_{v_{\rm tan}}$  is shown in Figure 14 (middle), where the majority of points are consistent with isotropic dispersions. We also compare our results to the parent population from Kim et al. (2019; open symbols), which shows that our subsample shows variation from the parent population, possibly due to selection effects. Our 1D tangential–to–line-of-sight velocity dispersions ( $\sigma_{v_{\rm 1D}}/\sigma_{v_r}$ ) show significant deviation from unity. The combined value for our total sample is  $\sigma_{v_{\rm 1D}}/\sigma_{v_r}=0.78\pm0.19$ . These measurements may indicate an elongation in the velocities along the line-of-sight direction.

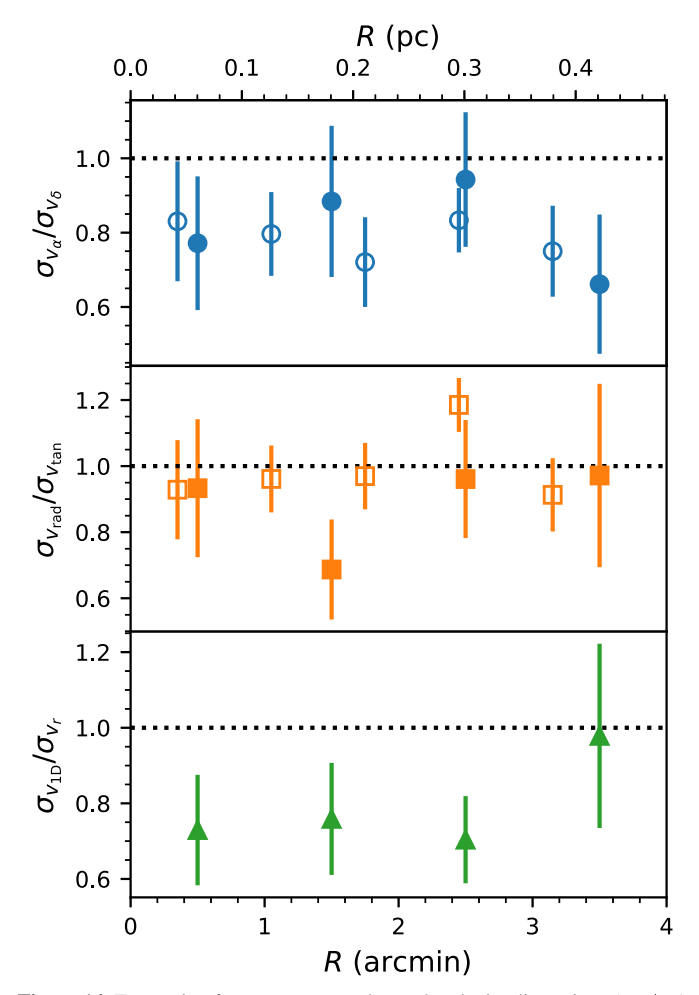
Platais et al. (2020) used a diagram of the angle of the PM vector in polar coordinates with respect to the cluster center to examine how the position vector from the center of the ONC and tangential velocity vector were related for fast-moving sources. The expectation is that runaway stars should have angles between these two vectors close to zero, that is, both the position vector and PM vector point radially away from the center of the ONC. We can use a similar analysis to see if there is preferential motion in the core of the ONC. Figure 15 shows the distribution of vectorial angles for all 135 sources in our sample with three components of motion. Random orbits should have no preferential angle; however, there is structure seen in Figure 15. Specifically, there is a preference for sources to have vectorial angles around  $90^{\circ}$  and  $-90^{\circ}$ . This corresponds to sources whose motion is tangential to a vector pointing radially away from the center of the ONC (normal vector), possibly indicating that there is a rotational preference for sources in the central ONC. In Figure 15 (bottom), we compare the cumulative distribution of vectorial angles for our 3D sample to the vectorial angles for all PM sources within 4' of the ONC CoM from Kim et al. (2019; 671 sources) and a random uniform distribution. The PM sample follows the expected behavior for a random uniform distribution of vectorial angles, which implies a potential bias within our 3D subsample.

To test for similarity between our 3D subsample and the parent PM sample from Kim et al. (2019), we performed the Kolmogorov–Smirnov (K-S) and Anderson–Darling (A-D) tests. The K-S test gave a test statistic = 0.115 with a p-value = 0.085, which indicates that we can reject the null hypothesis that the two samples come from the same distribution only at an 8.5% probability. The A-D test gave a test statistic = 0.802 with a p-value = 0.153, indicating that we cannot reject that these two distributions are significantly different, similar to the result of the K-S test. Neither of these test results are extremely significant, indicating that the resulting preferential motion of our 3D sample may not be statistically significant. However, it is worth noting the potential biases introduced into our 3D subsample versus the Kim et al. (2019) sample.



**Figure 13.** Plot of the 1D tangential velocity dispersion  $\sigma_{v,1D}$  (top), the line-of-sight velocity dispersion  $\sigma_{v_r}$  (middle), and the 1D velocity dispersion composed of all three velocity components (assumed isotropic)  $\sigma_{v,1D_{3D}}$  (bottom) as a function of distance from the center of the ONC. The values plotted are listed in Table 4, using an estimated distance to the ONC of  $388 \pm 5$  pc (Kounkel et al. 2017). The number of sources in each bin is indicated above that bin. The black solid line illustrates the 1D velocity dispersion for virial equilibrium predicted from the stellar and gas mass assuming a spherical potential from Da Rio et al. (2014), and the dashed lines mark the uncertainty assuming a 30% mass error. The bottom x-axis indicates distance in arcminutes, while the top x-axis indicates distance in parsecs.

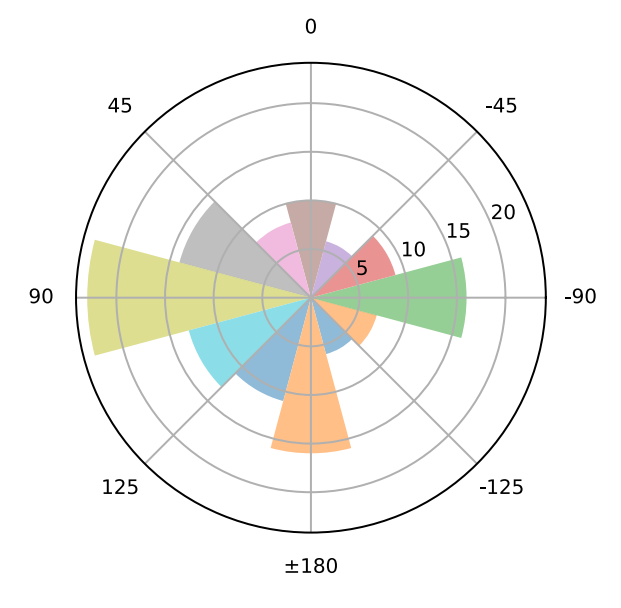
We also performed a comparison test against a random uniform sample using the same tests mentioned earlier. For our 3D subsample, the K-S test gave a test statistic = 0.126 with a p-value = 0.023, which indicates that we can reject the null hypothesis that the kinematic sample comes from a uniform

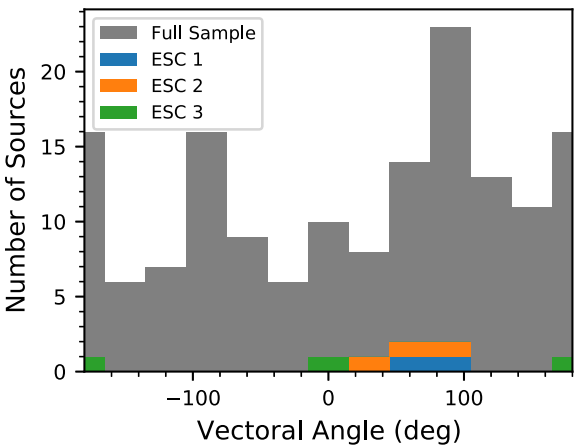


**Figure 14.** Top: ratio of east—west to north—south velocity dispersions ( $\sigma_{v_{tx}}/\sigma_{v_{ty}}$ ) as a function of distance from the core of the ONC. Open symbols are values from Kim et al. (2019), while filled symbols are from this study. There is a slight north—south elongation that has been found by other studies (e.g., Da Rio et al. 2014; Kim et al. 2019). Middle: ratio of radial to tangential (vectors on the plane of the sky pointing radially toward the center of the ONC and tangential to that vector) velocity dispersions ( $\sigma_{v_{Tad}}/\sigma_{v_{tan}}$ ). These components are primarily isotropic, with the exception of the bin between 1' and 2'. Bottom: ratio of tangential to line-of-sight velocity dispersions ( $\sigma_{v_{1D}}/\sigma_{v_r}$ ). There appears to be a slight elongation in the line-of-sight direction.

distribution at a 2.3% probability. The A-D test gave a test statistic = 1.786 with a p-value = 0.064, which indicates that the null hypothesis can be rejected at the 6.4% level. Again, neither of these test results are extremely significant, motivating the need for a larger kinematic sample within the core. Comparing the parent sample from Kim et al. (2019) to the random distribution gives a K-S test statistic = 0.019 with a p-value = 0.974 and an A-D test statistic = -0.892 with a p-value > 0.25 (value capped). Both tests indicate that the parent sample is consistent with a random distribution.

Our sample was selected for sources bright enough to be targeted with NIRSPAO (or APOGEE), likely selecting more ONC sources that are in the foreground portion of the cluster rather than deeply embedded sources, which may indicate motion differences as a function of depth in the ONC. Our target list was also curated from the [HC 2000] catalog, selecting sources preferentially thought to have masses  $\lesssim 1\,M_\odot$ . It is possible that lower-mass sources are showing different kinematics than the bulk motion within the ONC. Kuhn et al. (2019) attempted to measure the bulk rotation of the ONC





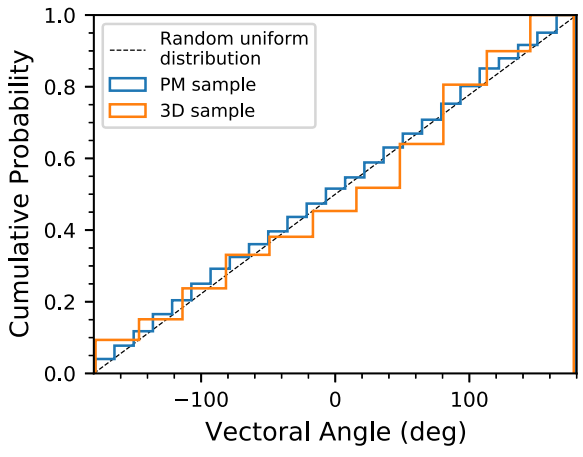


Figure 15. Top: polar histogram of the angle between the PM vector and the radial position vector on the plane of the sky, where an angle of zero corresponds to both the position vector and velocity vector pointing radially away from the cluster center. Each bin is 30° wide. The radial direction indicates the number of sources in each bin. There is an observed preference for sources to have motion tangential to the core of the ONC ( $\sim\pm90^{\circ}$ ), with more sources exhibiting motion of  $+90^{\circ}$  than  $-90^{\circ}$ . Middle: 1D histogram corresponding to the bins in the polar histogram. We show the vector angles of the escape groups identified in this study and Kim et al. (2019), noting that few of these sources have angles  $\sim0^{\circ}$ . Bottom: cumulative probability distributions for our 3D sample (orange), the entire PM sample within 4′ (blue), and the expected distribution for a random uniform sample (dashed line).

using tangential kinematics but found no significant rotational preference.

It is important to note that this analysis is done assuming all stars are at the same distance. The Gaia satellite (Gaia Collaboration et al. 2016) is currently obtaining parallaxes for over 1 billion sources; however, it has been noted in previous studies that Gaia measurements in the ONC are unreliable due to the high level of nebulosity (e.g., Kim et al. 2019). Indeed, the number of Gaia Early Data Release 3 (Gaia Collaboration et al. 2021) sources within 1" of our sources from this study and consistent within the  $2\sigma$  combined uncertainty in  $\mu_{\alpha}$  and  $\mu_{\delta}$  is only three sources. Therefore, a full 3D study of ONC kinematics is not yet possible and motivates the need for future facilities to obtain parallax measurements for ONC sources.

### 7. Conclusions

Using Keck/NIRSPAO, we have obtained high-precision RV measurements ( $\sigma \lesssim 0.5~{\rm km~s}^{-1}$ ) for a large number of sources within the core region of the ONC (41 sources within 1'). Additionally, we included a reanalysis of 172 ONC sources observed with SDSS/APOGEE. Using a combined sample of Keck/NIRSPAO, SDSS/APOGEE, and PM measurements from Kim et al. (2019), for a total sample of 135 sources, we presented a 3D study of the kinematics of the core population of the ONC. Our main takeaways are the following.

- 1. Our derived tangential IVDs of  $\sigma_{\nu_{\alpha}} = 1.64 \pm 0.12$  and  $\sigma_{\nu_{\delta}} = 2.03 \pm 0.13$  km s<sup>-1</sup> are consistent with previous results from the literature and the virialized model of the ONC from Da Rio et al. (2014).
- 2. Our derived line-of-sight velocity dispersion of  $\sigma_{v_r} = 2.56^{+0.16}_{-0.17}~{\rm km~s}^{-1}$  is slightly higher than the literature estimates. This is potentially due to our sources being concentrated more toward the core of the ONC, which may indicate that the core of the ONC is not yet fully virialized. We explored the possibility that binarity could play a role in creating our larger observed RV dispersions. We simulated different binary fractions from 0%–100% and their effect on the observed line-of-sight velocity dispersion. We found that almost any level of binarity could produce our observed velocity dispersion; however, only a very high level of binarity ( $\geq 75\%$ ) would make our line-of-sight velocity dispersion consistent with the observed tangential velocity dispersions. As the binary fraction for the ONC is estimated to be between  $\sim 10\%$  and 50% (e.g., Reipurth et al. 2007; Da Rio et al. 2017; De Furio et al. 2019), our larger observed RV dispersion is likely not caused by orbital motion in unresolved binaries and is more likely related to formation/evolution within the ONC.
- 3. We measure an elongation in the velocity dispersion along the line-of-sight direction compared to the tangential velocity dispersion,  $\sigma_{\nu_{1D}}/\sigma_{\nu_{r}}=0.78\pm0.19$ . This may indicate that there is structure to the velocities of stars in the ONC; possibly, it is a result of the "slingshot" mechanism from the background filament (Stutz & Gould 2016; Stutz 2018). The ratio of tangential velocity dispersions  $\sigma_{\nu_{\alpha}}/\sigma_{\nu_{\delta}}$  shows a north–south elongation that is consistent with previous studies (e.g., Da Rio et al. 2014; Kim et al. 2019) and tends to run along the filament. However, the tangential-to-radial (toward the

center of the ONC) velocity dispersions  $\sigma_{\nu_{\rm rad}}/\sigma_{\nu_{\rm tan}}$  appear consistent with unity, as other studies have noted (e.g., Da Rio et al. 2014; Kim et al. 2019).

- 4. We observe two additional potential kinematic outlier sources (escaping/evaporating) based on their RVs from APOGEE (2MASS 05351906-0523495 and 2MASS 05352321-0521357). However, their large line-of-sight velocities may also be due to binarity, and additional follow-up is needed to confirm if their velocities are truly elevated.
- 5. There is a somewhat low probability that the 3D sample is drawn from a uniform distribution, which could indicate a rotational preference on the plane of the sky, as indicated by the angles between the source position vectors and tangential motion vectors. However, the parent population of Kim et al. (2019) is consistent with a uniform distribution, i.e., no rotational preference. We find that both our 3D sample and the Kim et al. (2019) sample are relatively consistent; therefore, we cannot rule out the null hypothesis that both populations are consistent with a uniform distribution. A larger sample with higher-precision measurements is likely required to further investigate the bulk rotation of the ONC core.

Our study indicates that additional AO imaging and/or extremely high-resolution spectroscopy is necessary to increase the sample size and reduce uncertainties to determine if the core of the ONC is virialized and/or shows significant velocity structure. This will allow for a comprehensive study of the 3D kinematics of the ONC to better understand the difference between tangential and line-of-sight velocities. Future work is required to compare the data to detailed simulations (e.g., Kroupa 2000; McKee & Tan 2002, 2003; Proszkow et al. 2009; Krumholz et al. 2011, 2012; Kuznetsova et al. 2015, 2018) to determine the dynamical state of the ONC.

The authors would like to thank the anonymous referee for the incredibly valuable suggestions and comments that helped improve the impact of this manuscript. The authors would also like to thank observing assistants Joel Aycock, Heather Hershley, Carolyn Jordan, Julie Rivera, Terry Stickel, Gary Puniwai, and Cynthia Wilburn and supporting astronomers Greg Doppmann, Carlos Alvarez, Josh Walawender, Percy Gomez, Randy Campbell, Al Conrad, Alessandro Rettura, Jim Lyke, Luca Rizzi, and Hien Tran for their help in obtaining the observations. J.R.L. and D.K. acknowledge support from NSF AST-1764218, HST-AR-13258, and HST-GO-13826. J.R.L., Q.K., D.K., and C.A.T. are supported by NSF grant AST-1714816. This work is based on observations made with the NASA/ESA Hubble Space Telescope, obtained at the Space Telescope Science Institute, which is operated by the Association of Universities for Research in Astronomy, Inc., under NASA contract NAS 5-26555.

Support for this work was provided by NASA through NASA Hubble Fellowship grant HST-HF2-51447.001-A awarded by the Space Telescope Science Institute, which is operated by the Association of Universities for Research in Astronomy, Inc., for NASA, under contract NAS 5-26555.

Funding for the Sloan Digital Sky Survey IV has been provided by the Alfred P. Sloan Foundation, the U.S. Department of Energy Office of Science, and the Participating Institutions. The SDSS-IV acknowledges support and resources

from the Center for High-Performance Computing at the University of Utah. The SDSS website is www.sdss.org.

The SDSS-IV is managed by the Astrophysical Research Consortium for the Participating Institutions of the SDSS Collaboration, including the Brazilian Participation Group, the Carnegie Institution for Science, Carnegie Mellon University, the Chilean Participation Group, the French Participation Group, Harvard-Smithsonian Center for Astrophysics, Instituto de Astrofísica de Canarias, The Johns Hopkins University, Kavli Institute for the Physics and Mathematics of the Universe (IPMU)/University of Tokyo, the Korean Participation Group, Lawrence Berkeley National Laboratory, Leibniz Institut für Astrophysik Potsdam (AIP), Max-Planck-Institut für Astronomie (MPIA Heidelberg), Max-Planck-Institut für Astrophysik (MPA Garching), Max-Planck-Institut für Extraterrestrische Physik (MPE), the National Astronomical Observatories of China, New Mexico State University, New York University, the University of Notre Dame, Observatário Nacional/MCTI, The Ohio State University, Pennsylvania State University, Shanghai Astronomical Observatory, the United Kingdom Participation Group, Universidad Nacional Autónoma de México, the University of Arizona, the University of Colorado Boulder, the University of Oxford, the University of Portsmouth, the University of Utah, the University of Virginia, the University of Washington, the University of Wisconsin, Vanderbilt University, and Yale University.

Some of the data presented herein were obtained at the W. M. Keck Observatory, which is operated as a scientific partnership among the California Institute of Technology, the University of California, and the National Aeronautics and Space Administration. The Observatory was made possible by the generous financial support of the W. M. Keck Foundation.

The authors recognize and acknowledge the very significant cultural role and reverence that the summit of Maunakea has with the indigenous Hawaiian community, and that the W. M. Keck Observatory stands on Crown and Government Lands that the State of Hawai'i is obligated to protect and preserve for future generations of indigenous Hawaiians.

This research has made use of the Keck Observatory Archive (KOA), which is operated by the W. M. Keck Observatory and the NASA Exoplanet Science Institute (NExScI), under contract with the National Aeronautics and Space Administration.

Portions of this work were conducted at the University of California, San Diego, which was built on the unceded territory of the Kumeyaay Nation, whose people continue to maintain their political sovereignty and cultural traditions as vital members of the San Diego community.

Facilities: HST(ACS), Keck:II (NIRSPEC, NIRC2), Sloan (APOGEE).

Software: Astropy (Astropy Collaboration et al. 2013), emcee (Foreman-Mackey et al. 2013), corner (Foreman-Mackey 2016), NumPy (Harris et al. 2020), SciPy (Virtanen et al. 2020), Matplotlib (Hunter 2007), apogee (Bovy 2016).

## Appendix APOGEE Results

Table 5 shows the results of our forward-modeling pipeline applied to our APOGEE sources (see Section 4).

Table 5 APOGEE Forward-modeling Results

APOGEE ID	ID <sup>a</sup>	$\alpha_{\rm J2000}$	$\delta_{ m J2000}$	$\overline{RV}$	$\mu_{\alpha\cos\delta}$	$\mu_{\delta}$	$T_{ m eff}^{^{b}}$	v sin i	Veiling	Noted
		(deg)	(deg)	$(km s^{-1})$	(mas yr <sup>-1</sup> )	(mas yr <sup>-1</sup> )	(K)	$(km s^{-1})$	$\left(\frac{F_{H,\mathrm{cont}}}{F_{H,*}}\right)$	
2M05350101-0524103	663	83.75420833	-5.40286111	$31.46 \pm 0.19$	$0.16 \pm 0.07$	$-0.62 \pm 0.14$	$3825.01 \pm 12.53$	$38.23 \pm 0.92$	0.56	C
2M05350117-0524067	•••	83.75487500	-5.40186111	$25.59 \pm 0.18$			$3979 \pm 6$	$5.40 \pm 1.00$	0.51	
2M05350160-0524101	655	83.75666667	-5.40280556	$27.82 \pm 0.24$	$1.21 \pm 0.29$	$0.25 \pm 0.27$	$2908.02 \pm 9.21$	$35.18 \pm 0.88$	0.36	
2M05350284-0522082	140	83.76183333	-5.36894444	$25.49 \pm 0.14$	$-0.96 \pm 0.15$	$-1.85 \pm 0.31$	$5100.45 \pm 1.56$	$27.43 \pm 0.36$	0.58	
2M05350309-0522378	190	83.76287500	-5.37716667	$29.98 \pm 1.67$	$-0.20 \pm 0.38$	$1.01 \pm 0.05$	$3057.64 \pm 30.73$	$15.65 \pm 0.39$	0.39	
2M05350370-0522457	189	83.76541667	-5.37936111	$31.37 \pm 0.57$	$-0.13 \pm 0.48$	$-0.16 \pm 0.19$	$3138.91 \pm 23.35$	$12.69 \pm 0.50$	0.50	
2M05350437-0523138	11	83.76820833	-5.38716667	$24.65 \pm 1.29$	$0.42 \pm 0.16$	$0.95 \pm 0.05$	$4107.19 \pm 63.65$	$17.67 \pm 1.21$	1.04	
2M05350450-0523565		83.76875000	-5.39902778	$33.82 \pm 0.92$			$4591 \pm 7$	$27.77 \pm 1.63$	0.85	
2M05350461-0524424	657	83.76920833	-5.41177778	$26.44 \pm 0.44$	$0.12 \pm 0.10$	$-0.86\pm0.08$	$3988.02 \pm 9.04$	$16.79 \pm 0.40$	0.42	
2M05350481-0522387	67	83.77004167	-5.37741667	$26.95 \pm 1.16$	$0.63 \pm 0.01$	$1.26 \pm 0.11$	$3544.42 \pm 5.64$	$10.52 \pm 2.27$	0.67	
2M05350487-0520574	542	83.77029167	-5.34927778	$29.34 \pm 0.57$	$0.25\pm0.15$	$-0.23\pm0.25$	$3733.67 \pm 7.92$	$11.91\pm0.53$	0.62	

Notes. Table 5 is published in its entirety in machine-readable format. A portion is shown here for guidance regarding its form and content.

(This table is available in its entirety in machine-readable form.)

a ID number from Kim et al. (2019). b Continuum veiling causes extreme degeneracies with  $T_{\rm eff}$ . Caution should be taken when using derived temperatures with high veiling. c The H-band veiling parameter. d In this column, C = close companion to source ( $\lesssim 1''$ ), E3 = escape group 3, and V = RV variable source.

### ORCID iDs

Christopher A. Theissen https://orcid.org/0000-0002-9807-5435 Quinn M. Konopacky https://orcid.org/0000-0002-9936-6285 Jessica R. Lu https://orcid.org/0000-0001-9611-0009 Dongwon Kim https://orcid.org/0000-0002-6658-5908 Chih-Chun Hsu https://orcid.org/0000-0002-5370-7494 Laurie Chu https://orcid.org/0000-0002-1437-4463 Lingfeng Wei https://orcid.org/0000-0002-2612-2933

### References

```
Abel, N. P., Ferland, G. J., & O'Dell, C. R. 2019, ApJ, 881, 130
Abolfathi, B., Aguado, D. S., Aguilar, G., et al. 2018, ApJS, 235, 42
Alam, S., Albareti, F. D., Allende Prieto, C., et al. 2015, ApJS, 219, 12
Allen, P. R. 2007, ApJ, 668, 492
Astropy Collaboration, Robitaille, T. P., Tollerud, E. J., et al. 2013, A&A,
   558, A33
Baldwin, J. A., Ferland, G. J., Martin, P. G., et al. 1991, ApJ, 374, 580
Bally, J., Langer, W. D., Stark, A. A., & Wilson, R. W. 1987, ApJL, 312, L45
Bardalez Gagliuffi, D. C., Burgasser, A. J., Schmidt, S. J., et al. 2019, ApJ,
Bellini, A., Libralato, M., Bedin, L. R., et al. 2018, ApJ, 853, 86
Bernstein, R., Shectman, S. A., Gunnels, S. M., Mochnacki, S., & Athey, A. E.
   2003, Proc. SPIE, 4841, 1694
Berriman, G. B., Ciardi, D., Abajian, M., et al. 2010, in ASP Conf. Ser. 434,
   Astronomical Data Analysis Software and Systems XIX, ed. Y. Mizumoto,
   K.-I. Morita, & M. Ohishi (San Francisco, CA: ASP), 119
Berriman, G. B., Ciardi, D. R., Laity, A. C., et al. 2005, in ASP Conf. Ser. 347,
   Astronomical Data Analysis Software and Systems XIV, ed. P. Shopbell,
   M. Britton, & R. Ebert (San Francisco, CA: ASP), 627
Blake, C. H., Charbonneau, D., White, R. J., et al. 2008, ApJL, 678, L125
Blake, C. H., Charbonneau, D., & White, R. J. 2010, ApJ, 723, 684
Blake, C. H., Charbonneau, D., White, R. J., Marley, M. S., & Saumon, D.
  2007, ApJ, 666, 1198
Bovy, J. 2016, ApJ, 817, 49
Burgasser, A. J., Blake, C. H., Gelino, C. R., Sahlmann, J., &
   Bardalez Gagliuffi, D. 2016, ApJ, 827, 25
Butler, R. P., Marcy, G. W., Williams, E., et al. 1996, PASP, 108, 500
Carpenter, J. M. 2000, AJ, 120, 3139
Clark, B. M., Blake, C. H., & Knapp, G. R. 2012, ApJ, 744, 119
Cottaar, M., & Hénault-Brunet, V. 2014, A&A, 562, A20
Da Rio, N., Tan, J. C., Covey, K. R., et al. 2016, ApJ, 818, 59
Da Rio, N., Tan, J. C., Covey, K. R., et al. 2017, ApJ, 845, 105
Da Rio, N., Tan, J. C., & Jaehnig, K. 2014, ApJ, 795, 55
De Furio, M., Reiter, M., Meyer, M. R., et al. 2019, ApJ, 886, 95
D'Orazi, V., Randich, S., Flaccomio, E., et al. 2009, A&A, 501, 973
Duchêne, G., & Kraus, A. 2013, ARA&A, 51, 269
Duchêne, G., Lacour, S., Moraux, E., Goodwin, S., & Bouvier, J. 2018,
   MNRAS, 478, 1825
Dzib, S. A., Loinard, L., Rodríguez, L. F., et al. 2017, ApJ, 834, 139
Eisenstein, D. J., Weinberg, D. H., Agol, E., et al. 2011, AJ, 142, 72
Farr, B., Kalogera, V., & Luijten, E. 2014, PhRvD, 90, 024014
Fűrész, G., Hartmann, L. W., Megeath, S. T., Szentgyorgyi, A. H., &
  Hamden, E. T. 2008, ApJ, 676, 1109
Fischer, D. A., & Marcy, G. W. 1992, ApJ, 396, 178
Fischer, W., Edwards, S., Hillenbrand, L., & Kwan, J. 2011, ApJ, 730, 73
Foreman-Mackey, D. 2016, JOSS, 1, 24
Foreman-Mackey, D., Hogg, D. W., Lang, D., & Goodman, J. 2013, PASP,
Foster, J. B., Cottaar, M., Covey, K. R., et al. 2015, ApJ, 799, 136
Gaia Collaboration, Brown, A. G. A., Vallenari, A., et al. 2018, A&A, 616, A1
Gaia Collaboration, Brown, A. G. A., Vallenari, A., et al. 2021, A&A, 649, A1
Gaia Collaboration, Prusti, T., de Bruijne, J. H. J., et al. 2016, A&A, 595, A1
Gómez, L., RodrÍguez, L. F., Loinard, L., et al. 2005, ApJ, 635, 1166
Gray, D. F. 1992, The Observation and Analysis of Stellar Photospheres, Vol.
   20 (Cambridge: Cambridge Univ. Press)
Großschedl, J. E., Alves, J., Meingast, S., et al. 2018, A&A, 619, A106
Gunn, J. E., Carr, M., Rockosi, C., et al. 1998, AJ, 116, 3040
Harris, C. R., Millman, K. J., van der Walt, S. J., et al. 2020, Natur, 585, 357
Hillenbrand, L. A. 1997, AJ, 113, 1733
Hillenbrand, L. A., & Carpenter, J. M. 2000, ApJ, 540, 236
Hillenbrand, L. A., & Hartmann, L. W. 1998, ApJ, 492, 540
Hsu, C.-C., Burgasser, A. J., Theissen, C. A., et al. 2021b, ApJS, 257, 45
```

```
Hsu, C.-C., Theissen, C., Burgasser, A., & Birky, J. 2021a, SMART: The
  Spectral Modeling Analysis and RV Tool, v1.0.0, Zenodo doi:10.5281/
  zenodo.4765258
Hunter, J. D. 2007, CSE, 9, 90
Husser, T.-O., Wende-von Berg, S., Dreizler, S., et al. 2013, A&A, 553, A6
Jerabkova, T., Beccari, G., Boffin, H. M. J., et al. 2019, A&A, 627, A57
Johnson, H. M. 1965, ApJ, 142, 964
Jones, B. F., & Walker, M. F. 1988, AJ, 95, 1755
Karnath, N., Prchlik, J. J., Gutermuth, R. A., et al. 2019, ApJ, 871, 46
Kim, D., Lu, J. R., Konopacky, Q., et al. 2019, AJ, 157, 109
Kim, S., Prato, L., & McLean, I. 2015, REDSPEC: NIRSPEC Data Reduction,
  Astrophysics Source Code Library, ascl:1507.017
Köhler, R., Petr-Gotzens, M. G., McCaughrean, M. J., et al. 2006, A&A,
Kounkel, M., Covey, K., Suárez, G., et al. 2018, AJ, 156, 84
Kounkel, M., Hartmann, L., Loinard, L., et al. 2017, ApJ, 834, 142
Kounkel, M., Hartmann, L., Tobin, J. J., et al. 2016, ApJ, 821, 8
Kroupa, P. 2000, NewA, 4, 615
Kroupa, P., Aarseth, S., & Hurley, J. 2001, MNRAS, 321, 699
Kroupa, P., Petr, M. G., & McCaughrean, M. J. 1999, NewA, 4, 495
Krumholz, M. R., Klein, R. I., & McKee, C. F. 2011, ApJ, 740, 74
Krumholz, M. R., Klein, R. I., & McKee, C. F. 2012, ApJ, 754, 71
Kuhn, M. A., Feigelson, E. D., Getman, K. V., et al. 2014, ApJ, 787, 107
Kuhn, M. A., Hillenbrand, L. A., Sills, A., Feigelson, E. D., & Getman, K. V.
  2019, ApJ, 870, 32
Kuznetsova, A., Hartmann, L., & Ballesteros-Paredes, J. 2015, ApJ, 815, 27
Kuznetsova, A., Hartmann, L., & Ballesteros-Paredes, J. 2018, MNRAS,
  473, 2372
Lada, C. J., & Lada, E. A. 2003, ARA&A, 41, 57
Majewski, S. R., Schiavon, R. P., Frinchaboy, P. M., et al. 2017, AJ, 154, 94
Martin, E. C., Fitzgerald, M. P., McLean, I. S., et al. 2018, Proc. SPIE, 10702,
McKee, C. F., & Tan, J. C. 2002, Natur, 416, 59
McKee, C. F., & Tan, J. C. 2003, ApJ, 585, 850
McLean, I. S., Becklin, E. E., Bendiksen, O., et al. 1998, Proc. SPIE, 3354, 566
McLean, I. S., Graham, J. R., Becklin, E. E., et al. 2000, Proc. SPIE,
  4008, 1048
McNamara, B. J. 1976, AJ, 81, 375
Megeath, S. T., Gutermuth, R., Muzerolle, J., et al. 2016, AJ, 151, 5
Menten, K. M., Reid, M. J., Forbrich, J., & Brunthaler, A. 2007, A&A,
Moehler, S., Modigliani, A., Freudling, W., et al. 2014, Msngr, 158, 16
Muzerolle, J., Calvet, N., Hartmann, L., & D'Alessio, P. 2003a, ApJL,
  597, L149
Muzerolle, J., Hillenbrand, L., Calvet, N., Briceño, C., & Hartmann, L. 2003b,
    pJ, 592, 266
Nidever, D. L., Holtzman, J. A., Allende Prieto, C., et al. 2015, AJ, 150, 173
O'Dell, C. R. 2018, MNRAS, 478, 1017
Olivares, J., Sánchez, L. J., Ruelas-Mayorga, A., et al. 2013, AJ, 146, 106
Parenago, P. P. 1954, TrSht, 25, 3
Platais, I., Robberto, M., Bellini, A., et al. 2020, AJ, 159, 272
Prato, L., Mace, G. N., Rice, E. L., et al. 2015, ApJ, 808, 12
Proszkow, E.-M., Adams, F. C., Hartmann, L. W., & Tobin, J. J. 2009, ApJ,
  697, 1020
Raghavan, D., McAlister, H. A., Henry, T. J., et al. 2010, ApJS, 190, 1
Reggiani, M., & Meyer, M. R. 2013, A&A, 553, A124
Reggiani, M., Robberto, M., Da Rio, N., et al. 2011, A&A, 534, A83
Reipurth, B., Guimarães, M. M., Connelley, M. S., & Bally, J. 2007, AJ,
   134, 2272
Robberto, M., Soderblom, D. R., Bergeron, E., et al. 2013, ApJS, 207, 10
Robberto, M., Soderblom, D. R., Scandariato, G., et al. 2010, AJ, 139, 950
Rojo, P. M., & Harrington, J. 2006, ApJ, 649, 553
Sandstrom, K. M., Peek, J. E. G., Bower, G. C., Bolatto, A. D., &
  Plambeck, R. L. 2007, ApJ, 667, 1161
Schlafly, E. F., Green, G., Finkbeiner, D. P., et al. 2015, ApJ, 799, 116
Stutz, A. M. 2018, MNRAS, 473, 4890
Stutz, A. M., & Gould, A. 2016, A&A, 590, A2
Szentgyorgyi, A. H., Cheimets, P., Eng, R., et al. 1998, Proc. SPIE, 3355, 242
Tobin, J. J., Hartmann, L., Furesz, G., Mateo, M., & Megeath, S. T. 2009, ApJ,
  697, 1103
Tran, H. D., Mader, J. A., Goodrich, R. W., & Tsubota, M. 2012, Proc. SPIE,
  8451, 845129
van Altena, W. F., Lee, J. T., Lee, J. F., Lu, P. K., & Upgren, A. R. 1988, AJ,
van Dam, M. A., Bouchez, A. H., Le Mignant, D., et al. 2006, PASP, 118, 310
van Dokkum, P. G. 2001, PASP, 113, 1420
```

Virtanen, P., Gommers, R., Oliphant, T. E., et al. 2020, NatMe, 17, 261 Walker, M. F. 1983, ApJ, 271, 642 Walker, M. G., Mateo, M., Olszewski, E. W., et al. 2007, ApJS, 171, 389 Ward-Duong, K., Patience, J., De Rosa, R. J., et al. 2015, MNRAS, 449, 2618 Wen, Z., & O'dell, C. R. 1995, ApJ, 438, 784

Wilson, J. C., Hearty, F., Skrutskie, M. F., et al. 2010, Proc. SPIE, 7735, 77351C

Wizinowich, P. L., Le Mignant, D., Bouchez, A. H., et al. 2006, PASP, 118, 297

York, D. G., Adelman, J., Anderson, J. E., Jr., et al. 2000, AJ, 120, 1579